Vibrational Sum Frequency Generation Spectroscopy of Organic Semiconducting Thin Film Interfaces

A dissertation submitted to the University of Minnesota by:

Patrick Michael Kearns

In partial fulfillment of the requirements of the Doctor of Philosophy

Aaron Massari, Advisor

March, 2017

Acknowledgments

I would like to start off by thanking my parents Paul and Patricia Kearns, without whose continued support throughout my life and academic career I would not be here. Also, thanks to my brother Sean Kearns, with whom with I went to college and spent many hours studying for Michael Krische's organic chemistry class.

Thanks to the many teachers I have had through my life that have nurtured a lifelong love of science, of which this thesis is its greatest culmination so far. Specifically I would like to thank my high school chemistry teacher, Mrs. Carpenter, who first gave me a love for this discipline, and whose class was instrumental in preparing me for college. I would also like to thank Prof. Keith Stevenson, who let me spend two and a half years tinkering in his lab at the University of Texas. The opportunity he gave me made me realize that going to graduate school was a viable option with viable career oppurtunites. The work there was instrumental in preparing me for the rigors of graduate school.

I would thank the many people at the University of Minnesota who have helped me to get here. Thank you to the experimental physical chemistry super group for fostering a helpful and supportive community of researchers. Thank you to the members of the Massari Lab aswell. Dan O'Brien and Tim Anglin were instrumental in helping me to tackle the intense learning curve of nonlinear spectroscopy. Thank you as well to the members of the Massari group Brynna Jones, Zahra Sohrabpour, Chris Huber, Ivan Spector, Courtney Olsen, Cindy Pyles, and Isaac Prichett for help in the lab and on the laser, and for emotional support when I went crazy in our basement lab.

Finally I would like to thank the members of my committee for their time and input, David Blank, Donald G. Truhlar, C. Daniel Frisbie, and advisor Aaron Massari.

Aaron, thank you. You were a great advisor and scientist who taught me to be resourceful, work hard, and never take life too seriously.

In Dedication to Paul Kearns

“I’m just glad my kids didn’t become useless accounts or attorneys”-Paul Kearns C.P.A.

Abstract

This Dissertation is a compilation of my work done at the University of Minnesota in pursuit of a Ph.D. in Chemistry. The main theme is the use of vibrational sum frequency generation, an interface specific spectroscopic technique, to answer fundamentally interesting questions in the field of organic electronics, specifically the dielectric/semiconductor interface. This interface is of major importance in the function of organic field effect transistors. Chapters 1 and 2 will provide the relevant background on organic electronics and vibrational sum frequency generation, respectively. Chapter 3 is an explanation of the laser setup used to make the measurements. Chapter 4 explores the use of new modeling techniques to answer fundamental questions pertaining to the dielectric/organic interface under gate bias. Chapter 5 is the development of a new technique to collect multiple VSFG experiments at once. Finally, Chapter 6 uses techniques in both chapters 4 and 5 to examine how the organic semiconductor arranges itself on different gate dielectrics.

Table of Contents

List of Tables

Chapter 4: Optical Interference Enhances Nonlinear Spectroscopic Sensitivity: When Light Gives You Lemons, Model Lemonade

Chapter 6: Interfacial Spectra of PTCDI-C8 on Al_2O_3

List of Figures

Chapter 1: Introduction to Organic Field Effect Transistors

Chapter 2: Introduction to Vibrational Sum Frequency Generation Spectroscopy

Chapter 4: Optical Interference Enhances Nonlinear Spectroscopic Sensitivity: When Light Gives You Lemons, Model Lemonade

Chapter 1: Introduction to Organic Field Effect Transistors

1.1 Charge Transport in Organic Materials

When talking of charge conduction in materials band theory is often the first model introduced. One can think of a lower energy valence band of electrons bound to their nucleus. Above that a conduction band exists where the electron is no longer tightly bound to individual nuclei and is thus free to move in a particular direction under application of an electric field. In a band-type conductor, such as a metal, this valance band and conduction band overlap one another; promoting an electron from one to another takes less thermal energy than found at room temperature. This why these materials are room temperature conductors.[1]

In the case of insulators, the gap between the valence and the conduction band (the bandgap) is too large for electrons to be thermally excited into the conduction band. Between the extremes of conductors and insulators lie semiconductors. In a traditional semiconductor, the bandgap between valence and conduction bands is present but charge carriers, electrons or areas that lack electrons known as “holes,” can be thermally excited and promoted into valence band states that then conduct electricity.

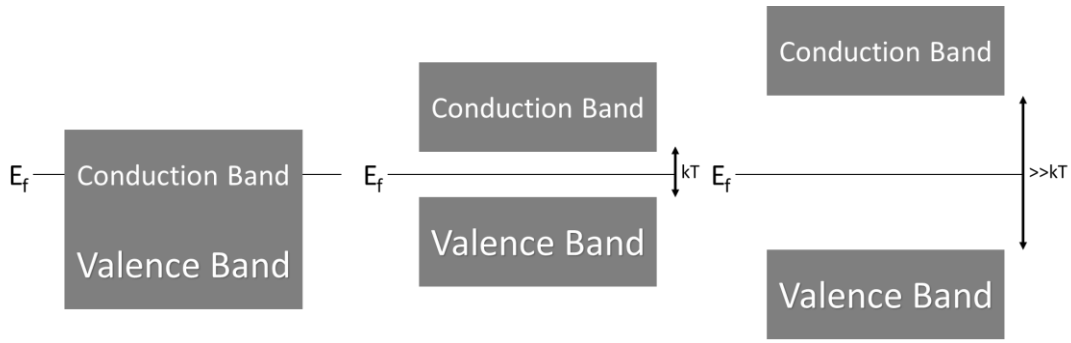

Figure 1.1: Diagram of a conductor where the partially filled conduction band straddles the Fermi level, a semiconductor where promotion of a charge carrier to the conduction band from the valence band is possible because the band gap is on the order of kT at room temperature, and an insulator where the band gap between valence and conduction bands are too large and the material does not conduct charge.

While band transport can be used to explain charge conduction in traditional inorganic semiconductors, as well as some highly ordered single-crystal organic semiconductors, it does not work well to explain charge conduction in most organic semiconducting materials. For these systems, we will have to first understand what makes organic semiconductors different from their inorganic counterparts. Structurally speaking, organic semiconductors are made up of organic (made of primarily carbon, nitrogen, oxygen, hydrogen, and sulphur) molecules or macromolecules (polymers). They typically have large regions of π conjugation that facilitate intra- and intermolecular charge delocalization.

Like inorganic semiconductors, organic materials can be separated broadly into either n-type, p-type, or amibipolar charge transporters. In inorganic as well as organic materials the p-type/n-type definition corresponds to whether the material transports primarily holes or electrons.

Most organic semiconductors are to some degree molecular crystals so packing will play a huge role in how the molecule behaves. Studies have shown that the most efficient transport occurs along the π-π stack of the material.[2] This means that for a material that aligns itself normal to a surface (edge-on) charge transport will be most efficient through a 2D layer in the direction of the stack and parallel to the surface.[2-3] This also means that the tilt of the molecules at the interface can greatly affect the efficacy of the device as this will affect how well the molecules are in registry with each other.[4-6]

Different models are needed to explain charge transport in organic materials because many are polycrystalline or amorphous. This relative disorder means that the traditional models of conduction do not work. There are broadly two models to explain charge transport: the polaron model, which is good for more ordered systems, and a charge hopping model, which is good for less ordered systems.[1-2, 7]

The polaron model works for a wide range of materials and temperatures.[8] A polaron is the charged moiety in the material and resultant deformation the surrounds the charged particle. This deformation can be of the delocalized π electron clouds surrounding the charged species as well as the molecular coordinates of the atoms in the surrounding molecules or even the lattice parameters of the crystal at large. In the organic materials under study here, the deformation is primarily that of the electron cloud and, depending on the material, the molecular coordinates.[1] Early studies by Kenkre et al. also showed how the model could be used to describe photoinduced electrons in naphthalene.[9] Polaron models have also been used to model the temperature effects of conductivity in pentacene.[10]

For more disordered systems a charge hopping model is used that draws inspiration from Marcus theory of charge transfer and then parameterizes it further.[2, 11]

Bässler and coworkers have done much in modeling the charge transfer properties of highly disordered organic semiconductors.[12-14] These models are very complex but work very well for highly disordered systems. In one case, a highly parameterized model was able to predict the carrier density dependence on charge mobility.[13]

In short, there are two categories of charge transfer models for organic polycrystalline thin films: either a polaron model that does not explicitly take into account charge transfer between two different states and just models charge transport though the material as a 'dressed charge', or a hopping model that more explicitly treats charge transfer as a hopping event subject to an Arrhenius type rate equation. Many of these hopping models also include the polarization induced in a material by the charge as is done in polaron models. The inherent strength in many of these models is that they can be parameterized and fit to account for experimental behavior. However, this means a true ab-initio theory of charge transport for a large range of different classes of materials is lacking.

1.2 Examples of Organic Semiconductors

A distinct advantage of organic semiconductors is that their properties can be readily modified by chemical synthesis. It is a long term goal of the field that by understanding the underlying fundamental forces that make a particular semiconductor perform well when compared to another to produce a better functioning organic semiconductor.

One widely studied class of p-type organic semiconductors is the acenes.[15] Tetracene and pentacene both show a great propensity under vacuum deposition and solution recrystallization to make large single crystals that perform very well as organic semiconductors. Tetracene can reach single crystal mobilities of up to 0.4 cm^2/Vs.[16]

Pentacene likewise can reach up to 75 cm^2/Vs, free carrier mobility.[17] Rubrene, a class of substituted tetracene is one of the best p-type semiconductors known with mobilities as high as 20 to 40 cm^2/Vs for single crystals.[18]

Anthony and coworkers have shown that the addition of the substituent triisopropylsilylethynl (TIPS) to pentacene leads to better packing and therefore transistor device performance. [19-24] TIPS is also shown to help with pentacene solubility and recrystallization.[21] Furthermore, substitution can be used to affect the electronic structure of pentacene more directly leading to interesting results. Dioxolane substitution leads to increased fluorescence as well as lowered ionization potential leading to easier charge injection in an organic field effect transistor (OFET) device.[19] Also, the substitution of electron withdrawing cyano groups turns pentacene in a suitable organic photovoltaic (OPV) acceptor.[24] Furthermore, Yassar and coworkers substituted cyano groups into terthiophene, and showed that this made it capable of n-type transport.[25] Marks and coworkers have also created oligothiophene based n-type semiconductors through substitution with fluorinated alkanes.[26-28]

There are fewer n-type organic semiconductors. These materials primarily transport negative charge carriers or electrons and are negatively charged while under device operation and therefore, many are not stable in air. N-type semiconductors when charged under normal device operation are more prone to reacting with oxygen and water leading to a chemical state that cannot conduct charge.[29] In fact, air stable n-type semiconductors are a longtime research goal.[29-33] Some examples include fullerene and fullerene derivatives. Fullerene has been reported to have an electron mobility of approximately 0.1 cm^2/Vs in vacuum.[34] The substituted fullerene, phenyl-C_{61}-butyric acid methyl ester (PCBM) has been reported to have mobilities as high as $1.6x10^2$ cm^2/Vs.[35] PCBM has the added of benefit of being soluble in most organic solvents.

Both of these materials also see use as acceptor materials in organic photo voltaic applications.[36]

Napthalenediimides show electron mobilities from very low, approximately 10^{-6} cm^2/Vs, to rather high at 0.16 cm^2/Vs, depending on substitution and whether they are under vacuum. Like many n-type conductors, device performance fades upon exposure to air.[37] Similar to the napthalenediimides and of special importance to this work are the perylenediimide derivatives. Based on substitution on the nitrogen of the imide group charge carrier mobility can be as high as 0.6 cm^2/Vs for PTCDI-c8 or around $6.9x10^{-5}$ cm^2/Vs.[38-39] It has been shown by several people that this change in mobility is from the packing of the different substituted molecules. The better performing materials taking on a more face-to-face packing arrangement.

In addition to small oligomers, several polymers show conductive and semiconductive behavior. The polythiophene class is probably the most well-known of the p-type semiconducting polymers. Of those, regioregular poly(3-hexylthiophene) (P3HT) is a very good conductor with a hole mobility reported to be around 0.2 cm^2/Vs.[40]. It has been shown that ultrathin films of regioregular P3HT self organizes into an edge-on arrangement at the interface.[41-42]

1.3 Device Integration

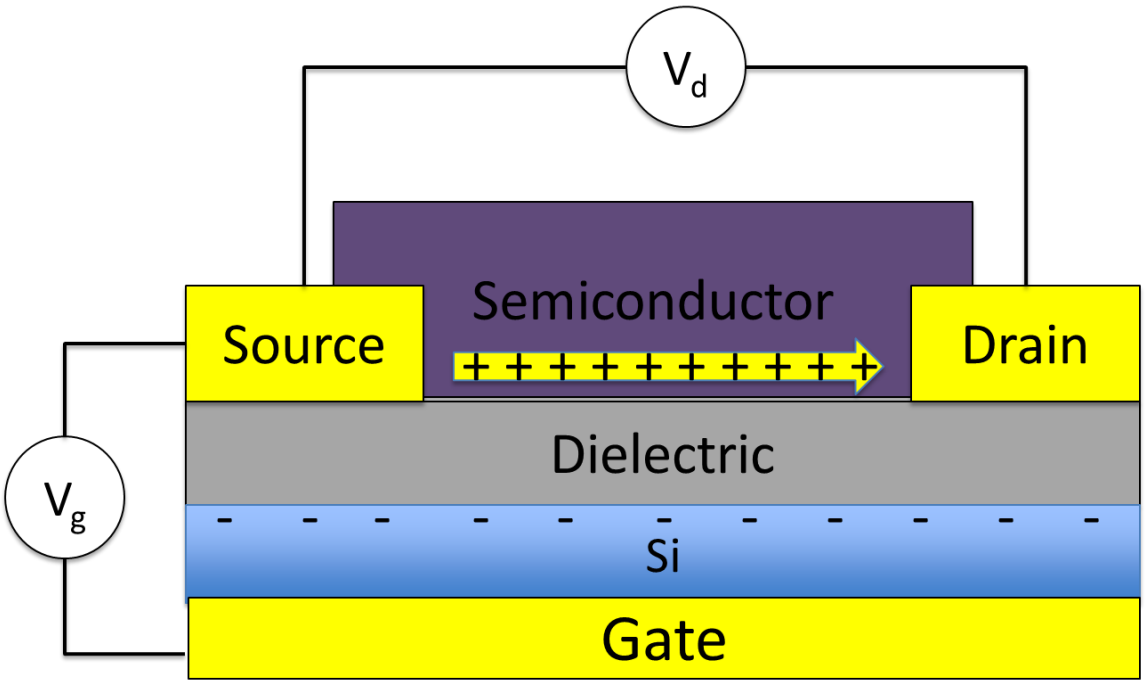

Figure 1.2: A typical bottom gate bottom contact organic field effect transistor (OFET). Under device operation a potential between source and gate (V_g) is applied, in this case negative, and charge builds up on either side of the dielectric. At the threshold bias (V_t), enough charge builds up in the semiconductor that for a given potential between source and drain (V_d) current will flow between source and drain (I_d).

The studies in this thesis primarily dealt with organic semiconductors as they are deployed in OFETs. There are several geometries of OFETs having to do with where the source, gate, and drain are located in relation to the semiconductor. There is top contact bottom gate, bottom contact bottom gate, and top gate bottom contact geometry (Figure 1.2). All devices in this thesis were bottom contact bottom gate geometry. This architecture is useful for our studies given that it allows us to deposit the metal

components all in a clean room facility doing photolithography and then deposit the organic material in our own lab. Also, this method gives a clear aperture in the sample to do spectroscopy experiments in the OFET charge carrying channel.

A transistor modulates the current passed between its source and drain electrodes (I_d) by varying the potential applied between the source and gate (V_g). In an OFET, a potential (V_d) is applied between the source and drain electroddes. A positive V_g will lead to negative charge being built up in the semiconductor material; a negative V_g will lead to a buildup of positive charges in the semiconductor. When a critical concentration of charge carriers has accumulated at a gate bias called the threshold voltage (V_t), charge conduction occurs. Then, for a given V_d across the channel, a characteristic I_d will flow between the source and drain (Figure 1.2).[1]

When examining the performance of an OFET the charge carrier mobility and threshold voltage parameters are often cited. The carrier mobility is a measure of how fast a charge will move for given electric field in the channel and has units of cm^2/Vs. The V_t, as described above, is the voltage at which current begins to flow from the source to the drain. [1] There are two experiments or regimes in which one can characterize a transistor to obtain these values. First, when V_g is much greater than V_d one is said to be operating in the linear regime. In the linear regime, the charge carrier density on the conducting channel is uniform across the channel (from source to drain). However, if V_d is on the same order of magnitude as V_g then one is operating in the saturation regime. The saturation regime is characterized by the depletion of charge carrier density near the drain. In the saturation regime, charge carrier density is not the same through the length of the channel (Figure 1.3).[1]

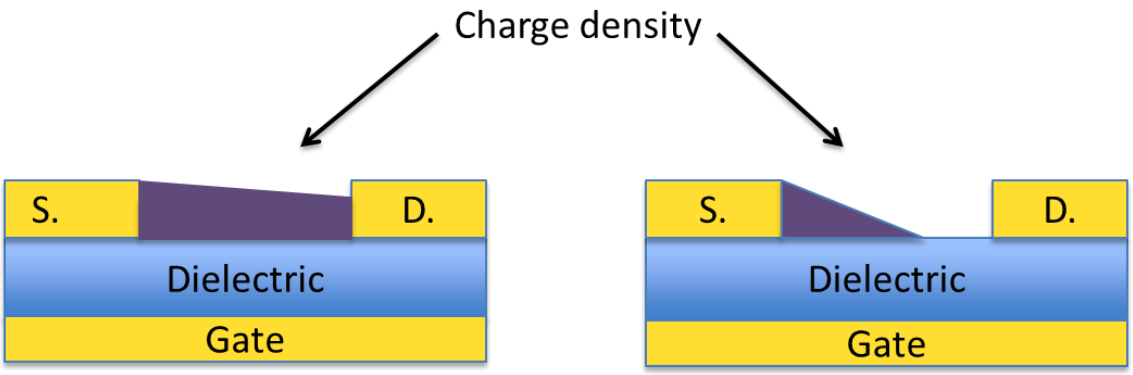

Figure 1.3: Diagrams of the charge carrier density in organic semiconductors along channel length under device operation, the linear regime on right and saturation regime on left. In the linear regime, V_d is much smaller than the V_g such that source and drain are near the same potential. Charge density along the channel is roughly constant. In the saturation regime, V_g and V_d are approximately the same, putting the drain at a much different potential than the source. When this occurs the charge carrier density around the drain becomes depleted.[1]

The names of the regimes are derived from how the I_d behaves under what is referred to as a transfer scan. A transfer scan is one of two experiments one can do to determine the threshold voltage and charge carrier mobility of a device. In a transfer scan the V_d is kept at a constant potential and the V_g is scanned either positive or negative depending of carrier type. In a transfer scan, the current remains near zero before the gate threshold voltage and then rapidly turns on in a linear fashion before leveling out in the saturation regime. In an output scan for a given V_g, the V_d is scanned and the drain current analyzed. In an output scan there is an initial linear increase followed by a point where current no longer increases. It should be noted that for the situation where many V_gs have been plotted against V_d a slice at a particular V_d will give you a transfer scan (Figure 1.4).[1]

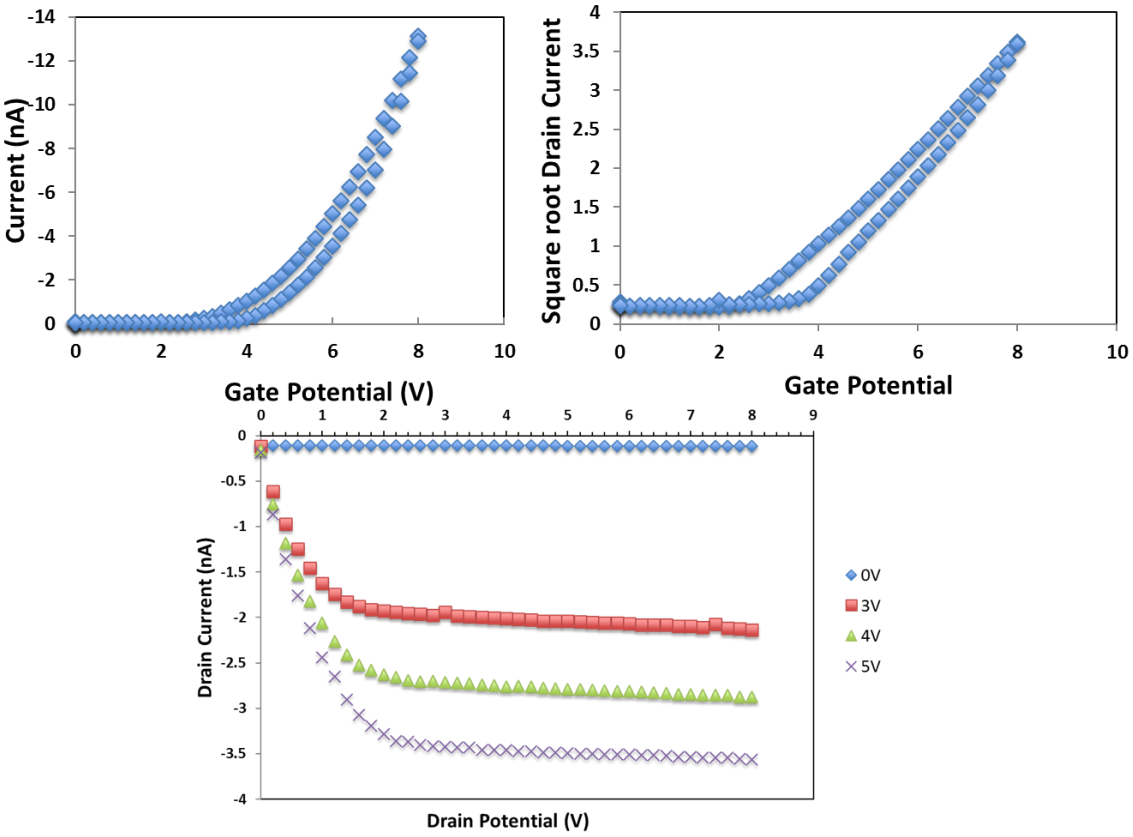

Figure 1.4: Above, transfer scans for a pentacene OFET device on A_2O_3 in the saturation regime. Top left are the data as collected, notice the parabolic nature of the drain current, which is linearized on the top right. V_t appears to be either 2 V or 4 V depending on direction. Below, is the same type of device in an output scan for multiple gate voltages. Notice 0 V is flat as the device does not turn on until approximately 2 V, and that at approximately V_d = 2 to 3 V the current remains largely flat as the saturation regime is entered.

In the linear regime, current can be represented as a function of the V_g or V_d per this equation.

$$I_d = \frac{W}{L}\mu C(V_G - V_T)V_{SD} \quad [1.1]$$

Notice that for a given V_d the I_d is linear with V_g. From a linear regression, the V_t and mobility can be determined.

When operating in the saturation regime[1-2]:

$$I_d = \frac{W}{2L}\mu C(V_G - V_T)^2 \quad [1.2]$$

The I_{dsat} is quadratic with respect to V_g. Taking the square root one can back out the V_t and mobility as well.

Using these methods, the mobility is convoluted with the effects of the contact resistance and the effects of non-constant charge distribution across the channel, which often leads to discrepancies among reported values for charge mobility.[1] Since the contact resistance is in series with the channel resistance, it can often be ignored when it is much less than the resistance through the channel. However, device dimensions can affect the relative magnitudes of channel and contact resistances. As the width of a channel is kept the same and the channel length is decreased, the channel resistance can become so small that the contact resistance is no longer negligible by comparison. Also if the width of the channel is increased relative to the length, the amount of contact can increase, again leading to the contact resistance no longer being negligible.[43]

Also of importance is contact geometry. Generally top contact geometry leads to devices with less contact resistance because the metal intercalates into the semiconductor leading to better contact. In systems where the metal is deposited first, as in bottom contact geometry used in this work, the metal affects how the semiconductor arranges itself leading to poorer contact.[43] The main conclusion is that contact resistance was not minimized in this work, but kept consistent so that the error would be systemic and results comparable. The devices made were never the high performing devices meaning the channel resistance dominated the mobility measurements, but they were designed to be self-consistent and reproducible.

1.4 Interfacial environment and device function

Inorganic semiconductors traditionally are made of homogenous single crystals. This means band transport can easily explain how conduction works. However organic semiconductors are often molecular crystals meaning the interactions between each molecule are much weaker than between the individual atoms in a Si crystal. Because of this, the hopping mechanism plays a large effect. This also means that molecular arrangement plays a huge role in how well the material acts as a semiconductor. For an organic semiconductor, the most efficient way charge is conducted is along the π-π stack between the molecules.[2] Because of this, molecules that pack themselves in an edge-on manner tend to make materials that perform better in OFETs than those that pack in other ways.

In an OFET device, the charge accumulation occurs in the first monolayer or two of the material on the dielectric meaning this dielectric semiconductor interface is critically important.[7] It has been shown that the outer morphology of the film has no correlation to device performance.[44-45] There have been many studies on how the

characteristics of the buried interface affect device performance.[44-50] Surface roughness has been shown to influence charge mobility with smoother dielectric surfaces producing better performing devices.[51] While roughness can increase grain boundaries leading to poorer performing devices several other studies have shown that it can have other effects as well.[46] One study by Knipp and coworkers examined how pentacene OFETs on rough silicon nitride compared to smoother SiO_2 dielectrics.[44] It was found that if the deposition characteristics were modulated to obtain comparable grain size of semiconductor on both the rough and smooth dielectrics, differences in the temperature dependent charge mobility could not be explained just from grain boundary traps. This led to the conclusion that the mobility differences were caused by surface scattering at the semiconductor/dielectric boundary. Yet another study by Steudel and coworkers examined the effects on charge mobility of pentacene OFETs using sputtered SiO_2.[47] Their reasoning for the decrease in device performance had to do with the presence of roughness valleys. Essentially, a charge would be in a topographical valley, experience a stronger potential and be trapped in the channel and not due to any change in grain size.

Self-assembled monolayers represent a useful way to modulate the interface between the semiconductor and the dielectric. The effects of SAMs and their mechanism of action have been studied extensively.[48-49] Salleo and coworkers did some of the first work on SAM treated dielectrics. In early studies, SiO_2 surfaces were treated with silane molecules. It was found that these surfaces provided better device performance than previous thin film polycrystalline transistors.[48] Specifically, SAMs with a permanent dipole were found to modulate threshold voltage. Kelley and coworkers did similar work on alumina dielectrics getting device performance on par with single crystal

devices.[49] The increase in performance was thought to be caused in part by the fact that the SAM made the surface much flatter.

SAMs with strong or at least permanent dipoles represent an interesting approach to modulate the dielectric interface. Work by Silas and coworkers showed that threshold voltage could be modulated using SAMs another way. They showed that SAMs with different net dipoles could shift V_t because the electric field induced by the dipolar SAMs either acted against or with the applied gate potential, increasing or decreasing the needed applied voltage to reach threshold.[50] Similarly, Fleischli and coworkers were able to improve V_t by application of SAMs that prevented charge transfer between the semiconductor and the dielectric surface.[45]

Despite all of the ways in which it can be modified, there are few methods to selectively and nondestructively characterize the buried dielectric and semiconductor interface. Many experiments either probe the outer interface or rely on destroying the system or delaminating the dielectric and semiconductor layers from each other.[52-57] Vibrational Sum Frequency Generation (VSFG) is a second order optical process that allows one to obtain a vibrational spectrum of a material at an interface. Specifically, it is a process that must occur in a non-centrosymmetric environment. Given that most these films are polycrystalline and thus randomly ordered, the only non-centrosymmetric environment is the interface. VSFG can reveal the relative orientation and ordering of the vibrational transition dipoles of the molecule at the dielectric surface. Many previous studies using VSFG have shown that the buried interface in a semiconductor dielectric system is different than the bulk material in a semiconductor.[58-61]. VSFG has become a valuable tool in looking at organic semiconducting materials, and will be the focus of the following chapter. [58, 61-69]

Chapter 2: Introduction to Vibrational Sum Frequency Generation Spectroscopy

VSFG is a powerful tool in determining key information about the orientation of molecules at the buried interface of OFETs. The following section will explain how and why VSFG works, as well as its technical limitations. Also, recent advances in data processing will be highlighted that allow one to surmount the unique challenges of using VSFG in this particular system.

VSFG spectroscopy involves the overlap in space and time of a broadband infrared (IR) laser pulse and narrow band visible pulse. The resultant signal is the sum of the energies of the two pulses. The signal is resonantly enhanced at the vibrational transitions of the system under study. This results in a vibrational spectrum that is upconverted into the visible wavelength region. This process can only occur in systems that lack centrosymmetry. In the case of the organic materials under study here, this can only occur at the organic semiconductor interface(s).

2.1 VSFG Surface Specificity

Spectroscopy is at its core the study of the interaction of light with matter. On the molecular level, we can describe the dipole of molecule under an electric field as the innate dipole of the molecule plus the oscillating dipole induced by an oscillating electric field of the incoming light [70]:

$$\boldsymbol{\mu} = \boldsymbol{\mu}_0 + \alpha \boldsymbol{E} \quad [2.1]$$

Here, **μ** is the total induced dipole, $\boldsymbol{\mu_0}$ is some inherent static dipole, and α is the polarizability of the molecule, the amount the dipole changes under a sinusoidally oscillating electric field, **E**. Under normal light intensities this effect as it is written above, is linear with **E**. It is under these levels of illumination (i.e. a light bulb or sunlight) that the phenomena of linear absorption and dispersion are observed.

However, under very high intensities the effects of light on the induced dipole are no longer linear and the induced dipole must be expanded in a power series[70]:

$$\boldsymbol{\mu} = \boldsymbol{\mu}_0 + \alpha \boldsymbol{E} + \beta \boldsymbol{E} + \gamma \boldsymbol{E} \ldots \quad [2.2]$$

where β is the hyperpolarizability and γ is the second order hyperpolarizability.

β is a molecular quantity. In the course of doing an experiment, many molecules will be observed and the ensemble average will be what is experimentally determined. To go from $\beta_{\alpha\beta\gamma}$ to the macroscopic quantity χ_{ijk} requires:

$$\chi_{ijk}^{(2)} = \frac{N}{\varepsilon_0} \sum_{\alpha\beta\gamma} \langle R(\psi) R(\theta) R(\varphi) \beta_{\alpha\beta\gamma} \rangle \quad [2.3]$$

in which χ_{ijk} is the ensemble averaged response of all the molecules in the area of the illumination by the laser. N is the total number of molecules under illumination, and the

bracketed terms represent an orientation average of all the molecules as they are transformed from the molecular coordinate frame to the lab coordinate frame via the Euler transformation matrices. $\chi^{(2)}$ is called the second order susceptibility and it is the macroscopic representation of the microscopic β.

For the purposes of sum frequency generation we need only look at the second order term in the induced polarization from two independently oscillating electric fields:

$$\boldsymbol{P}^{(2)} = \chi^{(2)}(\boldsymbol{E}_1 \cos(\omega_1 t) + \boldsymbol{E}_2 \cos(\omega_2 t))^2 \quad [2.4]$$

Upon expansion of the binomial the following terms appear:

$$\boldsymbol{P}^{(2)} = \chi^{(2)}(\boldsymbol{E}_1{}^2 + \boldsymbol{E}_2{}^2 + \boldsymbol{E}_1{}^2 \cos(2\omega_1 t) + \boldsymbol{E}_2{}^2 \cos(2\omega_2 t) + \frac{1}{2}\boldsymbol{E}_1\boldsymbol{E}_2 \cos((\omega_1 - \omega_2)t) + \frac{1}{2}\boldsymbol{E}_1\boldsymbol{E}_2 \cos((\omega_1 + \omega_2)t) \quad [2.5]$$

There are two terms with $2\omega_i$ arguments, which are known as the second harmonic generation (SHG) terms. There are two terms, $\mathbf{E}_1^2$ and $\mathbf{E}_2^2$, that do not oscillate in time at all; these are known as optical rectification. There is a term that oscillates at the difference of the two frequencies (ω_1-ω_2) that leads to difference frequency generation. Finally,there is a term that oscillates at the sum of the two input frequencies (ω_1+ω_2), which leads to sum frequency generation. The resultant oscillation in the dipole of the moiety under the electric field will then oscillate at the sum of the two input frequencies emitting an electric field that oscillates at that same frequency.

The direction that this component and all components emit are subject to phase matching conditions:

$$n_{sf}k_{sf}\sin\theta_{sf} = n_{vis}k_{vis}\sin\theta_{vis} \pm n_{IR}k_{IR}\sin\theta_{IR} \quad [2.6]$$

Where n is the refractive index of the material the beam is travelling through, k_i is ω_i/c, and θ_i is the angle with the surface normal. A positive operation is used for visible and IR beams propagating in the same direction; a negative operation is for beams traveling in opposite directions to the surface. The generated summed signal will be both reflected and refracted through the material where the summed signal originates. A picture of the direction the summed signal is emitted in relation to the input beams is provided in Figure 2.1.

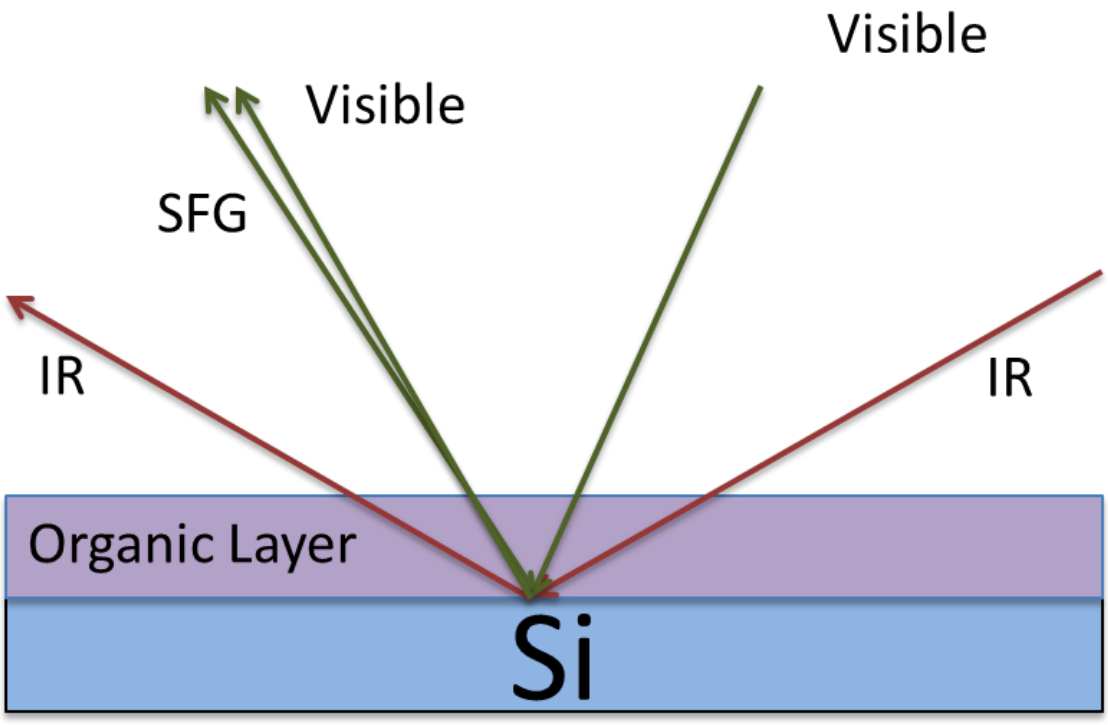

Figure 2.1: Depiction of co-propagating VSFG beam geometry. The IR and visible beams are reflected at the same angle they entered and the SFG signal is emitted at an angle closer the visible beam owing to phase matching conditions.

$\chi^{(2)}$ is a 3rd rank tensor and it is because of the nature of tensors that second order processes or indeed all even ordered processes are forbidden in centrosymmetric environments. Surface specificity occurs because a 3rd rank tensor has the mathematical property that negating all of the indices (inversion operation) must negate the sign of the quantity that it represents:

$$\chi^{(2)}_{i,j,k} = -\chi^{(2)}_{-i,-j,-k} \qquad [2.7]$$

However, in an environment that is centrosymmetric, the chemical environment and thus $\chi^{(2)}$ at one set of coordinates i,j,k and the $\chi^{(2)}$ at the inverse of those coordinates, -i,-j,-k, must be the same i.e.:

$$\chi^{(2)}_{i,j,k} = \chi^{(2)}_{-i,-j,-k} \quad [2.8]$$

For a centrosymmetric system the only way this is true is if $\chi^{(2)}$ is zero. Thus in a centrosymmetric environment $\chi^{(2)}$ is zero and therefore sum frequency generation forbidden. However, if we take two media that are perhaps both centrosymmetric, or both isotropic, the interface between the two will inherently be SFG active since it is not centrosymmetric.[70]

Furthermore this 27 element tensor can be simplified even more. In the case of two isotropic media in the xy plane meeting at the interface, only some of the $\chi^{(2)}$ tensor elements are nonzero. These elements are, assuming the plane is perpendicular to the x axis:

$\chi^{(2)}_{yyz}$	$\chi^{(2)}_{xxz}$
$\chi^{(2)}_{yzy}$	$\chi^{(2)}_{xzx}$
$\chi^{(2)}_{zyy}$	$\chi^{(2)}_{zxx}$
$\chi^{(2)}_{zzz}$	

Owing to the assumption of isotropy in the x-y plane some of these are equivalent specifically: $\chi^{(2)}_{yyz} = \chi^{(2)}_{xxz}$, $\chi^{(2)}_{yzy} = \chi^{(2)}_{xzx,}$ and $\chi^{(2)}_{zyy} = \chi^{(2)}_{zxx}$.[70]

The four nonzero independent elements of $\chi^{(2)}$ give us different information about the direction of a transition dipole in the molecule. They can be probed using different experiments that use different combinations of input linearly polarized light and

examining a specific output polarization. There are four experiments that can be performed with different polarization combinations. The SSP experiment $\chi^{(2)}_{yyz}$ the SPS experiment samples $\chi^{(2)}_{yzy}$, PSS samples $\chi^{(2)}_{zyy}$ and PPP samples a combination of all nonzero independent parts of $\chi^{(2)}$. The letters represent the polarization of the light in order of decreasing energy. In VSFG spectroscopy, this is summed signal first, visible input second, and mid-IR input third.[70]

2.2 Fitting VSFG Spectra

The observed VSFG signal can be fitted as the sum of several terms. Going back to equation 2.2. We see that the induced polarization is a result of the interaction of the electric field vectors with the second order susceptibility. Further breaking down equation 2.2 we can write the $\chi^{(2)}$ as a sum of a resonant and non-resonant portion:

$$\chi^{(2)} = \chi^{(2)}_{res} + \chi^{(2)}_{NR} \qquad [2.9]$$

Dealing with the resonant part first, this component will have all of the important chemical information relating to our molecule. Shen derived the entire response function from solving the density matrix using perturbation theory under the influence of the input and output electric fields and this derivation can be found in the literature.[71] The entire response function contains eight terms but can be simplified significantly under the conditions of typical VSFG, i.e. far from an electronic resonance and close to a vibrational resonance. Moad and Simpson and Shen reduced the expression down to:[72]

$$\beta^{ijk}(-\omega_{sum};\omega_a,\omega_b)_n = \frac{-1}{2\hbar}\sum_n \frac{\mu^k_{n0}(\alpha^{ij}_{0n})_{AR}}{(\omega_n-\omega_b-i\Gamma_n)} \qquad [2.10]$$

There are some interesting features in this equation. First, the resonant response has the form of a Lorentzian. The amplitude of that Lorentzian is the product of two factors, μ^k_{n0} and $(\alpha^{ij}_{0n})_{AR}$, which are the IR absorption cross section and anti-stokes Raman cross

section, respectively. This reveals the second selection rule of VSFG spectroscopy: for a transition to be VSFG active it must be both IR and Raman active.

The non-resonant component is typically taken to be a frequency independent offset with a complex phase factor. It is modeled in this work as:

$$\chi_{NR}^{(2)} = Ae^{-i\phi} \quad [2.11]$$

where A is the amplitude and φ is the phase. It will be shown in the next section how the complex nature of the resonant and non-resonant portions of the nonlinear response interfere in nonintuitive ways before being detected during the experiment.

Assuming the VSFG signal arises from a vibrational transition, the multiple elements of the $\chi^{(2)}$ tensor give the projection of the transition dipole onto those specific laboratory coordinates. Therefore, by performing different polarization experiments we can determine the average directionality of a transition dipole. There has been much work done on determining quantitatively the effect the transition dipole orientation has on the apparent magnitude of the observed signal measured in a particular polarization combination. This effect is complex and dependent on molecular symmetry,[72-73] however, a few qualitative determinations can be made. The ratio of the SSP signal to the PPP signal can be an indicator or how perpendicular a transition dipole is to the surface.[70] According to studies by Wang and coworkers, the orientation information given by the SPS and PSS experiment are the same.[73]

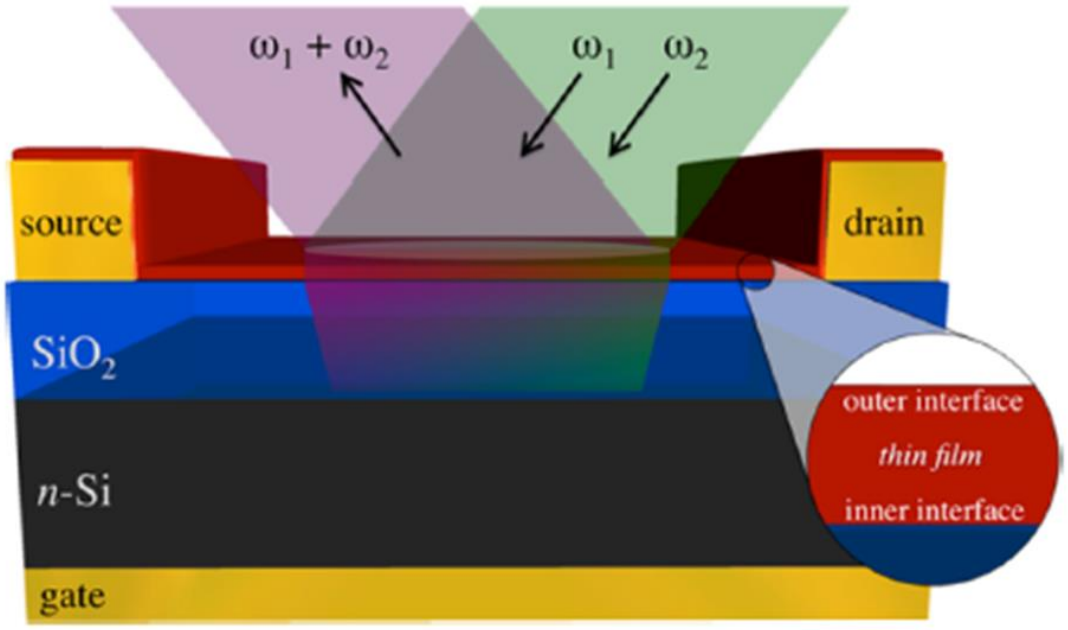

Figure 2.2: The source of thin film interference effects: there is laser overlap through the whole of the semiconductor layer generating signal from both the outer and the inner interfaces.

2.3 Thin Film Interference Effects

We now have a good understanding of $\chi^{(2)}$ and indeed how to model and fit it when it is observed in the data. We also know the deep orientational information that can be gleaned from it. It would seem then that analysis of the data after they are collected is relatively simple. This however is not the case. The many challenges and ways these challenges have been overcome will be the subject of the next section. Specifically, there are two major problems. Without absolute phase information, absolute orientation cannot be determined. Also, specific to the work done in this thesis, systems with multiple interfaces present unique challenges. VSFG is specific to interfaces, however, it is not specific to a specific interface. A problem in thin film organics is that there are often multiple signals from interfaces that can interfere with each other (Figure 2.2) Special modeling done to resolve this will be examined in later chapters

To fully understand how the various components of the nonlinear response affect each other, is important to understand what happens as the signal is detected. The generated electric fields are complex polynomials that are squared with their complex conjugates at the detector to produce a measureable intensity.

$$I_{IJK}^{SFG} \propto \left|\chi_{NR,IJK}^{(2)} + \sum_n \chi_{n,res,IJK}^{(2)}\right|^2 \quad [2.12]$$

The observed VSFG intensity is proportional to the absolute value squared of the sum of the complex resonant and non-resonant contributions. This is just a proportionality, there are important and complicated interactions in thin film experiments that are missed I this equation. It is necessary to take into consideration how the contributions of multiple interfaces interfere with each other as they are created at the interface and then pass through multiple films before exiting to the detector.

O'Brien developed a way to model these thin film interference effects.[74] What follows is a brief and simplified discussion of the thin film interference modeling.[75] The VSFG intensity after normalization to the input frequencies can be written exactly as:

$$I_0^{\alpha\beta\gamma} = \left|\sum_{v=1}^{n} T_v^{ijk} \chi_v^{(2),ijk}\right|^2 \quad [2.13]$$

In this equation, the intensity I, for a given polarization combination, α,β,γ, that is observed at the detector, is equal to the absolute value squared of the sum of all of the second order susceptibilitiess be they non-resonant or resonant, that contribute to that polarization combination, χ^{ijk}. Subscript *v* represents the layer in the dielectric stack of the material, starting at 1, the outer most material air interface, and going down n layers. For the modeling done in the studies presented here, this will include contributions from the outer, the first buried (semiconductor/dielectric), and the (dielectric/Si) interface.

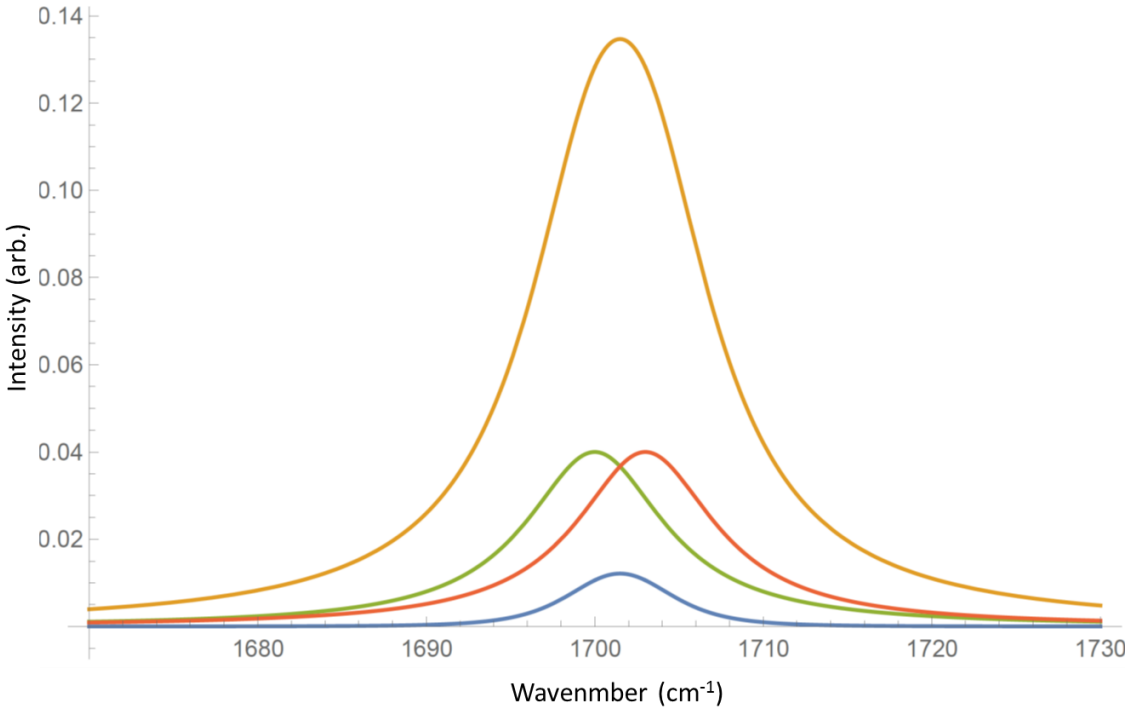

Figure 2.3: Simulated data showing the effects of interference on nonlinear signals: green and red curves show the absolute value of two Lorentzians centered at 1700 and 1703 cm^{-1}. If red and green have the same phase, orange results. If they have opposite phase, blue results.

As mentioned, the complex resonant and non-resonant contributions of the nonlinear susceptibility will interfere with each other at the instrument detector. Taking a simple situation of two resonant contributions of opposite phase and close in frequency, like what might happen in a situation where a material is deposited on a dielectric surface, ignoring any phase shift as the buried contribution travels though the material the two signals will destructively interfere with each other as they mix at the detector. This will reduce the apparent signal despite the fact that the contributing resonances are quite large (blue curve in Figure 2.3).[58] Similarly, if the two resonant contributions are close in frequency and have the same phase, then the two resonances will

constructively interfere and the resultant signal will be much larger than either resonance (orange curve in Figure 2.3).

The other new component of the equation is the transfer matrix, T^{ijk}. T^{ijk} is a frequency dependent value that is calculated for each material. It accounts for how the phase of the inputs and output signals phase will change as they travel through the many thin films in the system.[75-76] The phase of the buried signal will change as it travels through to material to the detector. This amount of phase change will be a function of the frequency dependent refractive index of the material that the signal is propagating through as well as the distance propagated, which is a function of the actual thickness of the material and the angle at which the signal is traveling. However, it becomes yet more complicated as the incoming IR or visible beams and the resultant VSFG signal beam will be by some fraction transmitted and reflected at each interface. The extent of reflection or transmission will again be a factor of both angle of incidence and refractive index contrast at the respective interfaces. This kind of refraction and reflection can continue indefinitely, and solving how such as system behaves is rather complex.

The thin film interference model developed by O'Brien models each interface with boundary conditions that must be consistent between all the available interfaces. What one is left with at the end is a matrix that needs the refractive index of all materials in the multi film stack, the thicknesses of those materials, and the incident angles of the visible and IR beams.[75-76] It was later shown that this model is very good at accounting for how thicknesses of materials in the multilayer stack, either the semiconductor or the dielectric, affect the apparent resonant signal of a material.[65-66]

In summary, an introduction to the major themes and problems of research in OFETs have been addressed with specific attention paid to the role the interface

between semiconductor and dielectric plays in the performance of the device. Specifically, surface energy, roughness, and chemistry have all been shown to have major effects on device performance leading to many studies on this interface. Some of the many approaches to its study, i.e. the use of x-rays, microscopy and more invasive methods have been highlighted. [52-57] Yet it was shown that these methods are lacking in that they either do not have the desired specificity to look only at the interface of the material or are destructive, making it impossible to examine the material as the device functions.

The fundamental principles governing VSFG were then discussed and the basis for its surface specificity and IR resonance enhancement were discussed. It was shown that the technique was quite effective at answering many questions regarding semiconductor/dielectric surface interactions. However, further advances were hamstrung by problems in the analysis of the data due to thin film interface effects. A new model was developed to deconvolute VSFG spectra of thin films, which was shown to be very effective.

The remainder of this thesis will be used to discuss recent advances made on this topic of VSFG spectroscopy on organic semiconducting thin films. Chapter 3 will describe the details of the VSFG instrument. Chapter 4 presents work done to model PTCDI-c8 on SiO_2 dielectric under gate bias. Analysis done using the thin film interference model reveals fascinating results that can only be revealed when taking into account thin film interference effects. Chapter 5 showcases an experimental development that uses multiple incoming visible beams to simultaneously obtain data for multiple polarization combinations at once. The work by O'Brien has shown that the thin film model is very sensitive to experimental conditions, having a way to perform multiple experiments at once reduces these effects. Finally, the experimental upgrades made

and the thin film model are used to examine the effects of PTCDI-C8 orientation and order at the interface of a new dielectric aluminum oxide and how it differs from SiO_2 in Chapter 6.

Chapter 3: Experimental Setup

The narrowband visible and broadband mid-IR pulse used to create the VSFG signal are made using a regenerative amplified Titanium Sapphire(Ti:Sapph) laser with approximately 30 nm bandwidth and 1W output at a 1 kHz repetition rate (Spitfire, Spectra Physics). The regenerative amplifier is seeded by a Ti:Sapph oscillator (Kapteyn-Murnane Laboratories) pumped by a frequency doubled neodymium vanadate laser (Millennium, Spectra Physics) with an output centered at approximately 800 nm with 50 nm of bandwidth and approximately 3 nJ per pulse. The regenerative amplifier is pumped by a Q-switched frequency doubled neodymium ytterbium lithium fluoride diode pumped laser (Empower 15, Spectra Physics) to produce approximately 2 W of uncompressed pulses centered at 800 nm. 500 mW of this is sent to a 4f pulse shaper described in more detail in Chapter 5. The remainder is compressed to approximately 40 fs to a 1 W output. 500 mW of that output goes to pump an optical parametric amplifier (OPA-300C, Spectra Physics).

The OPA signal and idler outputs are difference frequency mixed by a silver gallium sulfide crystal to create tunable mid-IR light approximately 2-3 μJ per pulse. The spectrally narrowed 1 nm bandwidth visible and broadband IR are focused onto the sample via off axis parabolic mirrors in co-propagating geometry. The visible and VSFG signal are then sent through a low-pass filter to remove the visible beam before being sent to a monochromator and attached liquid N_2 cooled CCD (Acton 2150i and Spec 10, Princeton Instruments).[61]

Chapter 4: Optical Interference Enhances Nonlinear Spectroscopic Sensitivity: When Light Gives You Lemons, Model Lemonade

4.1: Introduction

The chemistry of material interfaces often defines their function. When a reactant interacts with the surface of a solid catalyst, adsorption and reactivity are tuned by the unique kinetics and thermodynamics at the interface where bonding and nonbonding interactions are necessarily disrupted by the discontinuity of the bulk.[77-80] When charges are transferred across a metal-semiconductor interface, the energetics of the interfacial junction dictate the barriers for injection and transport.[81-84] Even for a solute in a homogeneous solution, the properties of the first solvation layer are different from the bulk liquid and it is the behavior of molecules in this solvent shell that largely affects the reactivity of the solute.[85-87] Interfaces are everywhere and identifying the influence of chemical structure and dynamics on their function is key to understanding how to control and improve their behavior.

As stated in Chapter 2, VSFG provides a selective and non-destructive way to probe the interfaces in a variety of different systems. VSFG has answered many fundamental questions about the interfacial structure of liquids,[88-93] metal-liquid junctions,[94-101] biological surfaces,[102-105] and environmentally-relevant materials.[106-107]

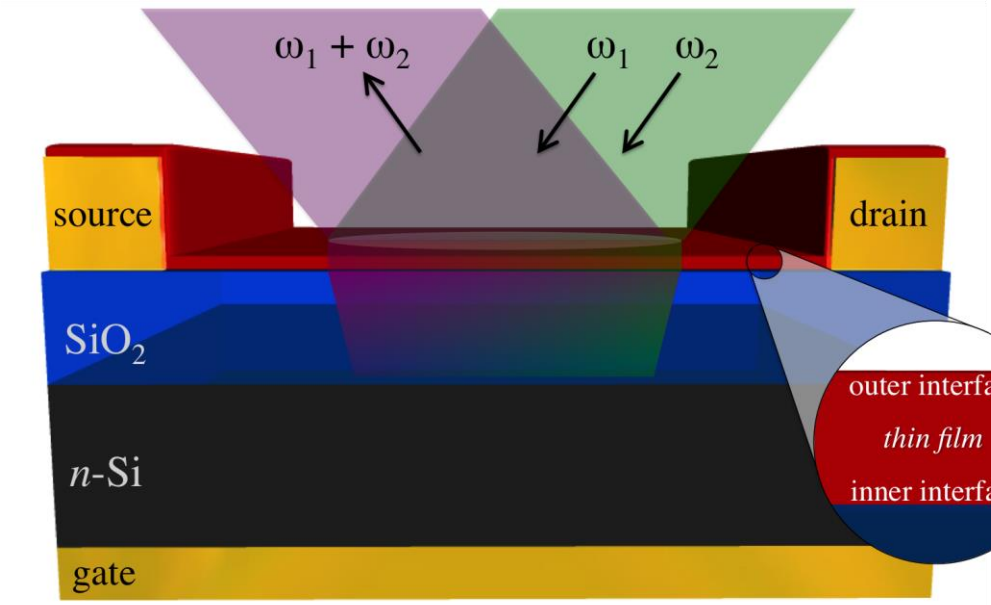

Figure 4.1. Schematic representation of a top-contact bottom-gated OFET, a layered stack of organic and inorganic films with multiple interfaces. Gate, source, and drain electrodes control transistor operation. VSFG input and output beams are shown with typical dimensions transmitting and reflecting between several interfaces. The upper and lower thin film interfaces (inset) are well within the focal volume of the pump beams.

The multiple interfaces in the thin film layers making up an organic field effect transistor (OFET, see Figure 4.1) make data analysis difficult due to thin film interference effects.[65, 75-76] Historically, many VSFG reports have chosen to ignore the influence of multiple interfaces. In some cases, this is justified by very large film thicknesses that move the second interface well outside of the focal volume of the driving fields, or strongly attenuate one of the three beams by absorption. In other instances, beam angles and polarizations have been used to minimize one of the two signals, effectively favoring one interface over the other by total internal or external reflection.[108-110] This approach can be effective for specific systems and beam polarizations, but the

evanescent field penetration remains the limiting factor and, for most thin film thicknesses (tens to hundreds of nm), both interfaces will still be sampled. Even when the signal from one interface is small, its interference with the signal from the other interface may still be significant. An additional complication is that the optical coefficients for most materials rarely allow one to minimize signal from one interface for multiple beam polarizations, which are needed to obtain structural information by VSFG.[74, 76]

A different approach to the problem is to fully model the interference of incoming and outgoing beams in the VSFG experiment and to leverage the sensitivity of the mixed signals to identify subtle changes in film properties. This has been carried out by a few groups treating wave propagation as a series of reflection and transmission events, generally from systems composed of a single thin film.[109-112] Work by O'Brien in our group has showed that the transfer matrix formalism provides a highly accurate approach to this modeling that is generalized to systems composed of any number of thin film layers.[65-66, 74, 76] It can be used to predict VSFG spectra and extract structural information from both interfaces of any thin film layer within the system, as was described in Chapter 2. This has inspired a different perspective on VSFG multilayer interference in our lab, and motivated us to move towards modeling, rather than avoiding, optical interferences in VSFG signals in order to gain exquisite sensitivity to the interfaces.

To underscore the strength of the modeling approach, the work in this chapter demonstrates how multilayer interference can be used to extract small spectroscopic changes that occur at only one of two thin film interfaces. The system of interest is an OFET that is electrically biased to accumulate charge carriers (electrons, in this case) at the organic-dielectric interface. The geometry of this multilayered device is shown in Figure 1. When a gate voltage is applied, injected charges rapidly accumulate at the

dielectric interface where they are driven laterally between source and drain electrodes.[113] The source-drain current flows primarily through a monolayer of the organic semiconductor directly adjacent to the dielectric surface, making molecular structure and charge delocalization in this interfacial region key factors in determining charge transport efficiency.[113] The interfacial nature of charge accumulation in the OFET provides an ideal system to study the impact of changes at only one thin film interface since the outer interface is unaffected by device activation.

In principle, the vibrational frequency of the imide symmetric stretch on PTCDI should serve as a spectral reporter of the fractional charge that is localized on the average perylene moiety. Gas phase calculations predict red-shifts of nearly 50 cm^{-1} for these modes on the PTCDI anion. However, in practice, the vibrational frequencies of organic molecules in the conduction channel of OFETs are almost never reported to shift in response to charge accumulation.[114-117] One exception exists to our knowledge, and in that case the anionic PTCDI species was only observed after a chemical reaction occurred to transfer a counter ion from a gel dielectric into the semiconductor thin film.[117] In reality, a small fractional charge is likely to be present on each molecule leading to a relatively small frequency perturbation that may be below the resolution of most VSFG instruments.

4.2: Experimental

Sample Preparation

Samples were prepared by photolithographic patterning of source and drain electrodes on silicon wafers purchased with the thermally grown and polished oxide dielectric (University Wafer). These were cleaned following the RCA protocol detailed elsewhere.[58] The PTCDI was vapor deposited through a shadow mask onto the

transistor channel with the substrate held at 30°C and post annealed at 110°C in a homebuilt vapor deposition chamber. Resulting in a device with bottom gate bottom contact geometry as seen in Figure 1. Transistor channel dimensions were 1 × 1 mm. The capacitance of these devices was measured to be 1.19×10^{-8} F/cm^2.

VSFG setup

The VSFG instrument setup has been described in chapter 3.[61] Spectra were collected in the ssp polarization. PTCDI is generally considered an n-type organic semiconductor, which makes these thin films susceptible to oxidation from environmental oxygen and water.[37] A vacuum cell suitable for placement in the VSFG spectrometer was designed and fabricated at the University of Minnesota. The cell includes windows for input and generated beams and three vacuum ports: one for actively pumping on, a second for an electrical feed-through to make connections to OFETs under study, and a third for a vacuum pressure gauge.[74] This allowed for applied biases to OFETs with in-situ VSFG studies under high vacuum.

VSFG spectra were averaged over a series of five exposures of 4 minutes each with a 4 minute background acquired with the mid-IR blocked. Spectra were collected on transistor devices at the following gate voltages in order: 0, -80, -10, 0, 10, 20, 30, 40, 50, 80, 100, 0, -80, 0 V.

Density functional theory calculations

Density functional theory calculations were performed on various substituted PTCDI molecules in Gaussian 09 using the B3LYP functional and 6-311++g (d, p) basis set. Geometry optimizations were performed at lower basis sets and slowly built up to the 6-311++g (d, p) level of theory.[118] The IR frequencies were calculated at the same level of theory as the geometry optimizations. CM5 population analyses of the molecules were also performed on the “core” of the molecule, as defined in Table 4.3.[119-122] The charges on the substituents attached to the nitrogen were ignored and the total

charge on just the PTCDI core was determined. The results were then plotted on a graph of frequency vs. excess charge on the core.

The substituents of PTCDI that were explored by DFT were aliphatic and a nitrile. These substituents were chosen to span a range of fractional charges on the core from 0 to -1 since PTCDI undergoes n-type transport during OFET operation. Substituents were chosen to be similar to the alkyl side chains in the PTCDI-C_8 used in the experimental work in this study. The resulting carbonyl stretching vibrations in the substituted PTCDIs were visualized to verify there was negligible coupling with vibrations in the chosen substituents. This was done to ensure that the change in fractional charge on the PTCDI core was due solely to the donation of electron density to the core as a result of the substituent and not due to geometric or coupling effects. Chains containing F, O, OH substituents and N were tested but excluded for this reason. In those cases, changes in the total charge of the molecule would lead to charge changes on the perylene core but would not change the frequency of the carbonyl vibration.

Simultaneous Fitting Procedure

The raw data were modeled at the electric field level and thin film interference effects as described in Chapter 2 were taken into account. Contributions to the observed signal were modeled as a non-resonant background, and four total Lorentzian resonances for the asymmetric (v_{as}) and symmetric (v_s) stretches at the inner and outer interfaces.[76]

The resonant portions of the nonlinear susceptibility, $\chi_{v,q}^{(2),yyz}$, were modeled as Lorentzian oscillators:

$$\chi_{v,q}^{(2)} = \frac{A_{v,q}}{\omega_{v,q} - \omega_{mIR} - i\Gamma_{v,q}} \qquad [4.3]$$

$A_{v,q}$ is the amplitude of the Lorentizian oscillator, $\Gamma_{v,q}$ is the oscillator HWHM, $\omega_{v,q}$ is the resonant frequency, and ω_{mIR} is the frequency of the infrared light. The nonresonant susceptibility $\chi^{(2)}_{\mathrm{NR}}$ does not vary with IR frequency but is complex and can be expressed in polar form as:

$$\chi^{(2)}_{\mathrm{NR}} = A_{\mathrm{NR}} e^{-i\phi} \qquad [4.4]$$

in which A_{NR} and ϕ are the nonresonant amplitude and phase, respectively. The nonresonant signal is treated as an effective susceptibility that has absorbed the effects of thin film interferences because the source of the nonresonant response is not well-characterized.

In fitting the spectra, the transfer matrix, T_v^{yyz}, for each interface v, were known from previous work[76] and the $\chi^{(2),\mathrm{yyz}}_{v,q}$ were parameterized to fit the data as follows. All of the VSFG spectra in Figure 2 were fitted simultaneously with the frequencies, widths, and amplitudes for the outer interface symmetric and asymmetric carbonyl stretches shared at all potentials but allowed to float. The inner interface frequencies and amplitudes for both modes were adjusted independently for all 8 gate potentials. The nonresonant magnitude and phase were also adjusted independently. The relative phases for inner and outer contributions of the same mode were kept opposite one another as well as the relative phase between the symmetric and asymmetric stretch on the same interface as described previously.[65-66, 76] The same peak width was used for the asymmetric and symmetric stretches at both interfaces but allowed to float.

4.3 Data Analysis

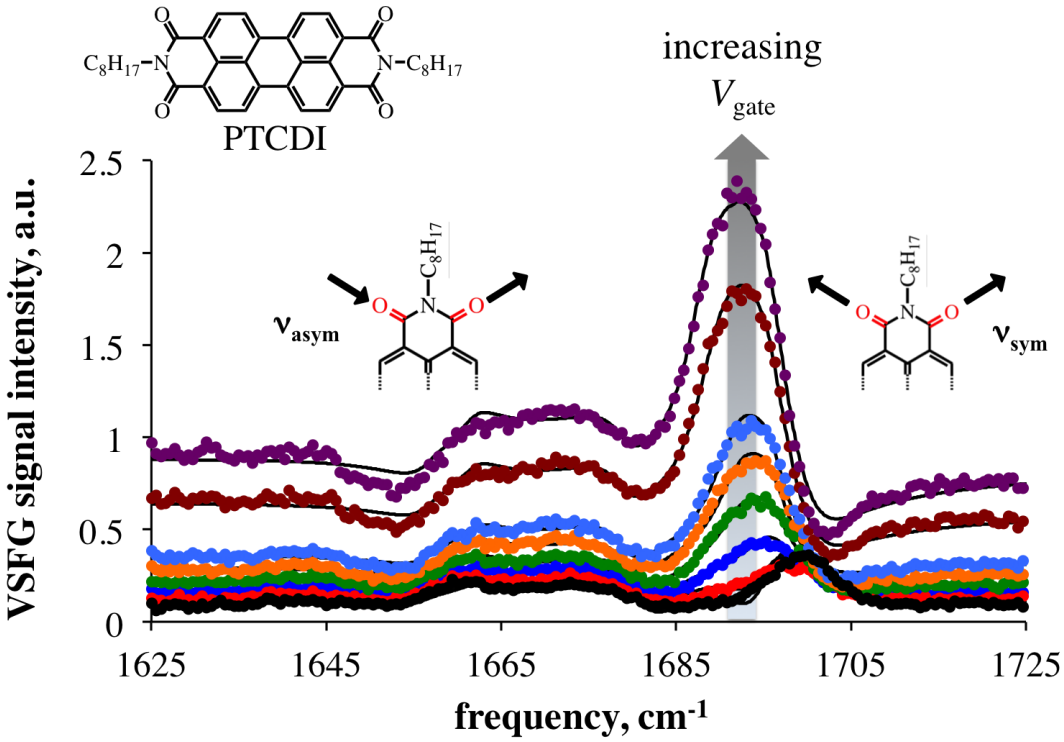

Figure 4.2. VSFG spectra in the imide vibrational region collected with an ssp polarization combination from a PTCDI (shown inset) transistor during gate bias (V_{gate}) for accumulation of electrons. Spectra shown are for V_{gate} values of 0, 10, 20, 30, 40, 50 , 80, and 100 V color coded in black, red, blue, green, orange, aqua, brown, and purple, respectively. Inset shows the structural basis for the asymmetric (ν_{asym}) and symmetric (ν_{sym}) stretching modes. Overlaid on each spectrum is the calculated fit using the multilayer interference model.

Figure 2 shows how the VSFG spectrum in the imide vibrational region changes as the gate bias increases from 0 to 100 V. The spectra in this frequency range are characterized by a broad vibrationally non-resonant offset and the imide carbonyl symmetric (ν_{sym}) and asymmetric (ν_{asym}) stretching modes. The non-resonant

background is the result of electric field enhancement and indicates carrier accumulation at the interface and formation of an interfacial electric field.[61, 123-126] The asymmetric stretch is quite weak for this polarization combination (ssp) and will not be the focus of our analysis. Qualitatively, the ν_{sym} at ~1690 cm^{-1} shows an initial red-shift at low gate biases, but then appears to increase in *intensity* with no obvious frequency shift. If we were to think of this as a single interface system, a common explanation would be that the film has undergone an increase in polar order or orientation as the charge density increased. However, this interpretation is incorrect since all interfaces between PTCDI, the dielectric, and the gate electrode fall within the focal volume of the driving fields, and both the PTCDI-air and PTCDI-dielectric interfaces possess ν_{asym} and ν_{sym} resonances that are VSFG-active. The VSFG spectra are the direct result of multilayer interference of the incoming and outgoing beams.

Table 4.1. Best fit parameters for asymmetric stretch (ν_{as}) and non-resonant background from global fit to VSFG spectra.

gate bias (V)	ν_{as} (cm^{-1})		$A_{as} \times 10^4$		Γ (cm^{-1})	A_{NR}	ϕ_{NR} (rad)
	outer	inner	outer	inner			
0	1656.41	1681.43	2.886	5.702	3.94	0.3174	1.1439
10		1681.01		5.383		0.3567	1.1270
20		1681.21		4.515		0.4108	1.0860
30		1680.77		3.898		0.4706	1.1436
40		1679.09		3.378		0.5341	1.3517
50		1678.94		3.323		0.5921	1.3804
80		1678.98		2.571		0.7877	1.3868
100		1678.92		2.323		0.9241	1.4107

Table 4.2. Best fit parameters for symmetric stretch (ν_s) from global fit to VSFG spectra.

gate bias (V)	ν_s (cm^{-1})		$A_s \times 10^3$		Γ (cm^{-1})
	outer	inner	outer	inner	
0	1692.31	1693.49	2.54	2.99	3.94
10		1693.18		2.74	
20		1692.46		2.66	
30		1691.70		2.62	
40		1691.17		2.50	
50		1690.71		2.13	
80		1689.11		1.81	
100		1688.19		1.63	

Tables 4.1 and 4.2 show the best fit results of this analysis. Notably, all of the spectra in Figure 2 were readily fit with shared parameters for the outer interface resonances at all gate biases, consistent with the fact that the outer interface is unaffected during OFET activation. The calculated spectra from the global fit are overlaid on the spectra in Figure 4.2 as black lines and show excellent agreement. After deconvoluting the interfacial responses from interference effects, the vibrational spectra are recovered as in Figure 4.3 for the outer and inner interfaces.

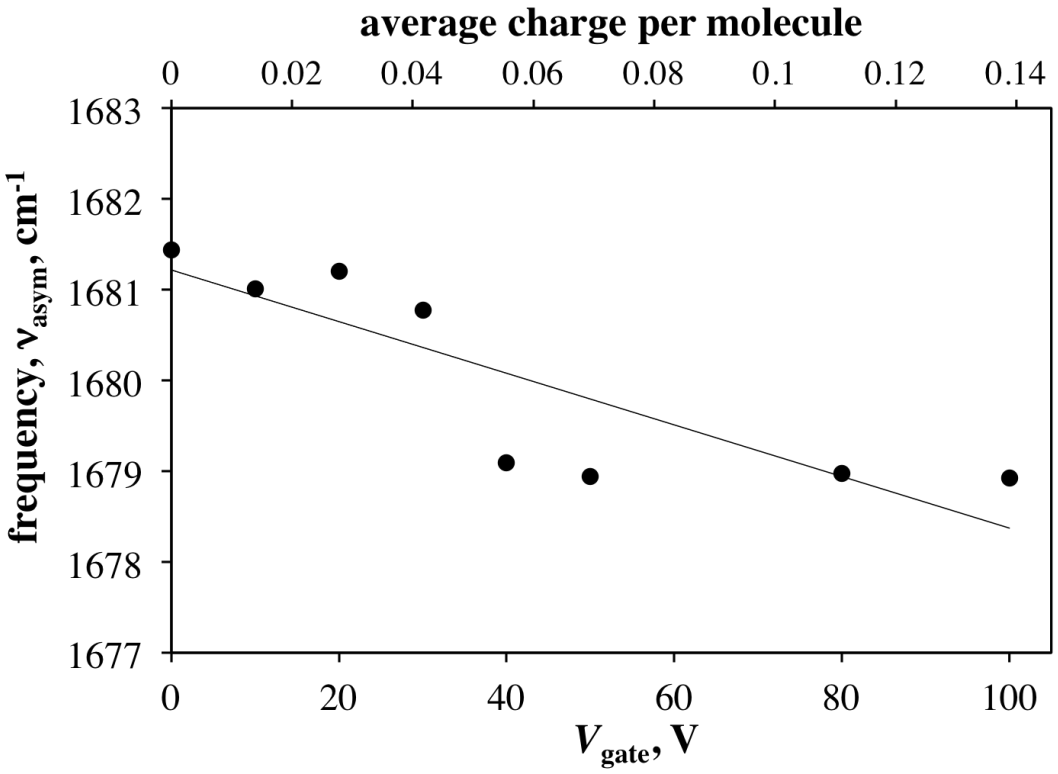

Figure 4.3. Best fit parameters for the inner (buried) interface imide asymmetric stretching frequency as a function of applied gate bias. Note that the average charge per molecule was derived as described in the main text, using the ν_s mode rather than the ν_{as}.

The asymmetric stretching region (1650 to 1680 cm^{-1}) was fit to two resonances for PTCDI at the outer and inner interfaces. Although it was fit in the same way as the symmetric region, the uncertainty from the low signal makes any in-depth analysis difficult. However, it is important to note that the v_{as} resonances affect the overall fit of the data as they interfere with the nonresonant and symmetric stretch at the electric field level. The outer interface frequency and amplitude were shared at all potentials and fit to 1656.4 cm^{-1} and approximately 0.0003. The inner frequencies and amplitudes were different for every potential; however, the frequency was found to be around 1680 cm^{-1} under all conditions. Figure 4.3 shows the center frequency of the inner v_{as} as a function of applied potential demonstrating its gradual decrease with voltage. Over this voltage range, the amplitude decreases by about a factor of three. Comparing Table 4.1 to Table 4.2, the amplitudes of the asymmetric stretch were fit to be an order of magnitude smaller than the symmetric stretch. Also, the inner and outer v_{as} are separated by 20 cm^{-1}, which is much more than might be expected. There is certainly a fair amount of error on these frequency values given the signal-to-noise of the spectra in this region.

In the case of the symmetric stretching mode, while the observed VSFG signal of the v_s region appears to increase as potential is increased, the actual value for the buried amplitude *decreased* as potential was increased (see Table 4.2). This illustrates the effects that thin film interference can have on the observed signal versus the actual strength of the interfacial oscillator. In this case, despite the fact that the observed signal strength of the symmetric stretch increased, the buried portion actually decreased.

The apparent increase in the amplitude of the symmetric stretch is actually a result of the shift in frequency of the buried interface as well as interference with the increasing nonresonant contribution. The resonances of the inner and outer v_s were fit

to similar amplitudes. The frequency of the buried symmetric stretch red-shifts as the gate potential is increased. As the inner contribution of the symmetric stretch shifts farther from the position of the outer contribution they interfere with each other and with the nonresonant background more constructively, resulting in an overall increased resonant signal.

Typically, a change in the VSFG intensity of vibrational mode can be related to either a change in interfacial order or orientation if there is a corresponding increase in the output from another polarization combination. Other polarization combinations were not analyzed here so it can only be said that the decrease is likely caused by some kind of structural change at the interface that increases with potential.

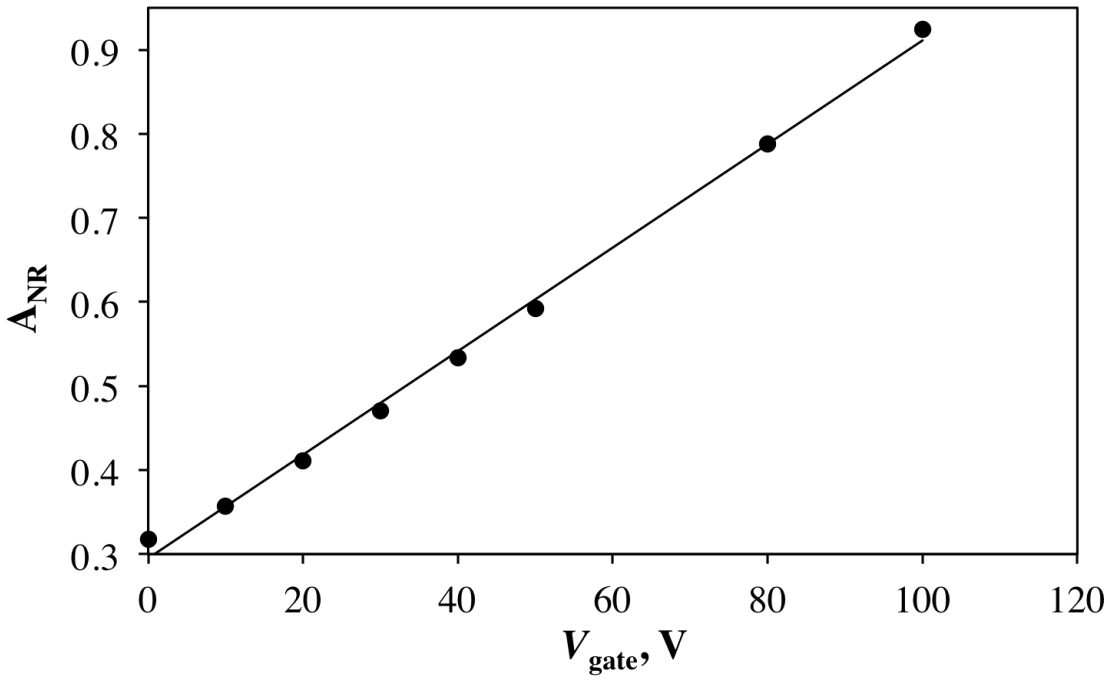

Figure 4.4. Non-resonant amplitude from global fit of gate bias-dependent VSFG spectra increases linearly due to charge accumulation at the buried interface.

The magnitude of the nonresonant signal increases linearly (slope = 0.0062 V^{-1}) as potential is increased (see Figure 4.4). This is expected as a portion of the nonresonant signal is from the electric field created at the dielectric surface and PTCDI surface that is increasing due to charge accumulation.[61, 125] The nonresonant susceptibility is predicted to increase linearly with the DC electric field strength.[61, 125] The nonresonant phase showed neither large changes nor a correlation with applied gate bias. Previous work showed that the phase of the nonresonant signal will undergo a rapid π phase shift as the polarity of the applied potential is changed.[61] However, in this work the polarity was always positive, therefore we would not expect any large changes in the direction of the interfacial electric field.

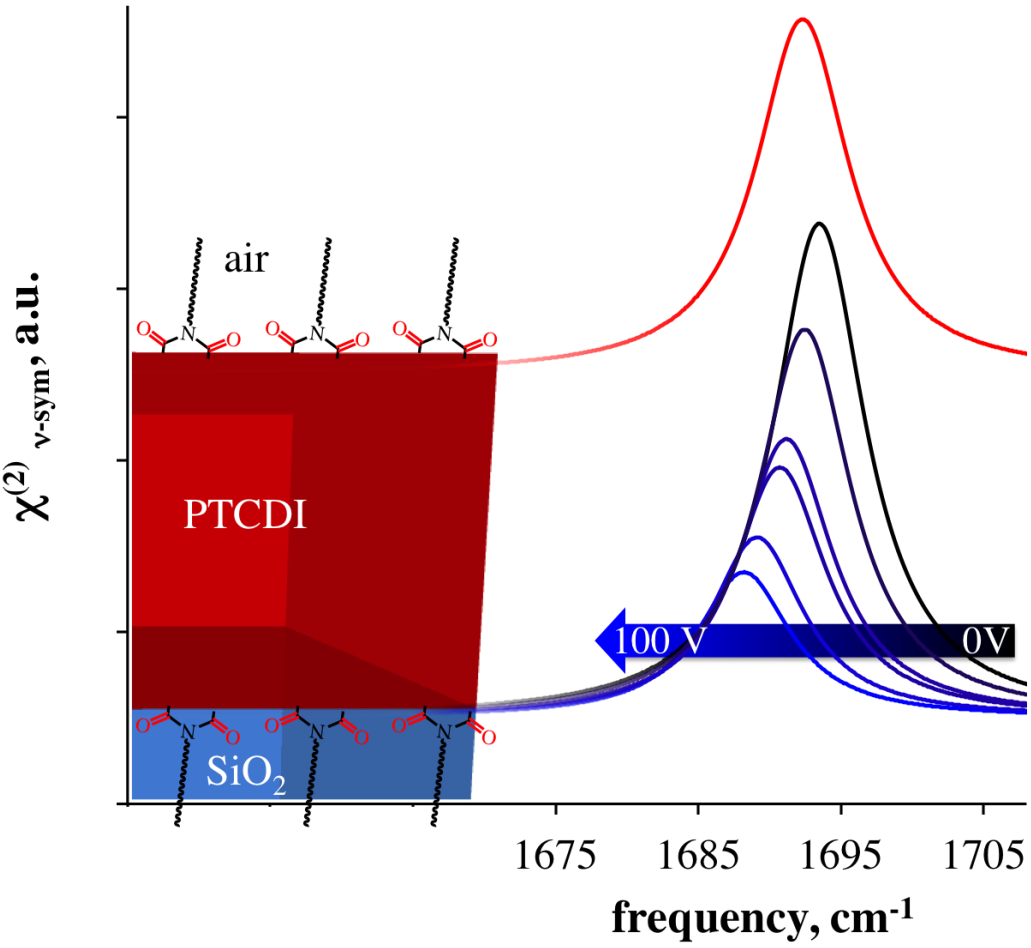

Figure 4.5. Extracted $\chi^{(2)}$ spectra for the ν_{sym} at the outer (red) and inner (black to blue) interfaces, as shown schematically to the left in the frame.

This example illustrates the profound influence that thin film interference can have on the observed VSFG signal (Figure 4.5). Even though the amplitude of the buried ν_{sym} decreases, the frequency shift and multilayer interference cause the inner and outer interface VSFG signals along with the nonresonant background to interfere more constructively. The outcome indicates a loss of polar order and/or orientation and a linear decrease in the average frequency of the imide symmetric stretching vibration with increased charge accumulation. This is the *opposite* of the single interface interpretation offered above, but multilayer interference modeling of VSFG spectra from

layered materials is a more complete and accurate treatment of the data. Intuition may not always the best metric for accuracy, especially at surfaces where the energetics often cause molecular behavior to defy expectations,[127] but in this case, it is intuitive that injected charges would disrupt interfacial order at the buried interface.

Table 4.3: Calculated frequency of the symmetric imide vibration for various substituents on the perelyne core, for the overall positive, neutral and negativily charged moiety.

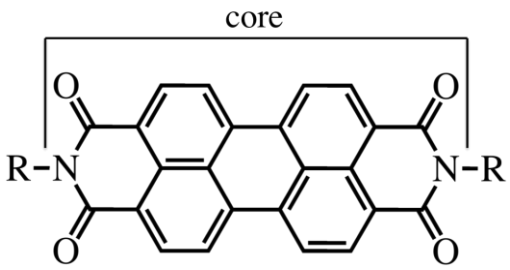

····R	charge type	calculated v_s (cm^{-1})	charge on core	experimental v_s (cm^{-1})
	double anion		-2	1606[128]
	anion	1646.09	-1	1642[128]
····H	neutral	1697.50	0	1688[129] 1696[128]
	cation	1714.96	1	
	anion	1634.45	-1.36	
····CH_3	neutral	1688.29	-0.45	1692[130]
	3cation	1703.81	0.46	
	anion	1633.48	-1.33	
····CH_3	neutral	1687.32	-0.44	
	cation	1699.93	0.46	
	neutral	1687.32	-0.43	
····CH_3	anion	1633.00	-1.32	
	anion	1652.88	-1.15	
····CH_2	neutral	1697.99	-0.28	
	cation	1705.26	0.58	
····C_8H_{17}	anion		-1.32	1629[117]
	neutral		-0.43	1696[117]
	anion	1667.43	-1.1	
····C≡CH	neutral	1666.46	-0.18	
	cation	1724.66	0.71	
	anion	1680.04	-0.90	
····C≡N	neutral	1696.05	-0.03	
	cation	1741.64	0.90	

A linear regression fit to the buried interface data indicates a decrease of 0.054 cm^{-1} per V. To translate this red-shift into a fractional charge per molecule, we can establish the expected frequency shift per unit charge from the results of the gas phase DFT calculations. Table 4.3 shows the calculated v_s frequencies (scaled by a factor of 0.97)[131] for a variety of substituted PTCDI species. Also included are experimental frequencies for dimethyl-PTCDI,[130] unsubstituted PTCDI,[129] adamantylthio-substituted PTCDI,[128] and PTCDI-C_8 anion and neutral forms.[117] These data were plotted in Figure 4.6, and the core charges for the experimental frequencies were taken to be the same as the calculated values for the same molecule. An exception was the adamantylthio-substituted PTCDI, which did not converge computationally and was simply assigned core charge values of 0, -1, and -2. The calculated frequencies are in good agreement with experimental results.

The data were fit to a straight line. Work by others had shown linear behavior for vibrational frequencies with fractional charge.[132] As electrons are either added to the anti-bonding LUMO or removed from the HOMO of the PTCDI core, they will affect the frequency of the bond in a proportional way. On initial examination this seems to hold, the nitrile group leads to a fractional charge of -0.0251 and resonance for the carbonyl symmetric stretch of 1696 cm^{-1} while the more electron donating ethyl group leads to a charge of -0.444 and a frequency 1687 cm^{-1}. The ethyl and acetyl groups are less electron donating with charges of -0.282 and -0.1825, but their frequencies do not follow this trend with the ethyl substituted and acetyl substituted PTCDIs having resonances at 1697 cm^{-1} and 1666 cm^{-1}, respectively. However, when ethyl functionalized PTCDI is ionized into anion or cationic form the overall trend is maintained with the charges and frequency for cationic, neutral and anionic ethyl substituted PTCDI being: 0.584 and 1705 cm^{-1}, -0.282 and 1697 cm^{-1}, and -1.146 and 1652 cm^{-1}, respectively. The results for acetyl substituted PTCDI seem to not follow the trend with: 0.712 and 1724 cm^{-1}, -

0.183 and 1666 cm^{-1}, and -1.06 and 1667 cm^{-1}. Between the neutral and anionic forms the trend breaks down for the acetyl substituted PTCDI. This could mean there is something other than charge density on the PTCDI core effecting frequency of the carbonyl bond. Notwithstanding these uncertainties, there is still a strong linear trend of the overall data (see Figure 4.6). The data were fitted to a line with a slope of 39.2 cm^{-1} /charge and a y-intercept of 1694 cm^{-1} with an R-squared value of 0.86.

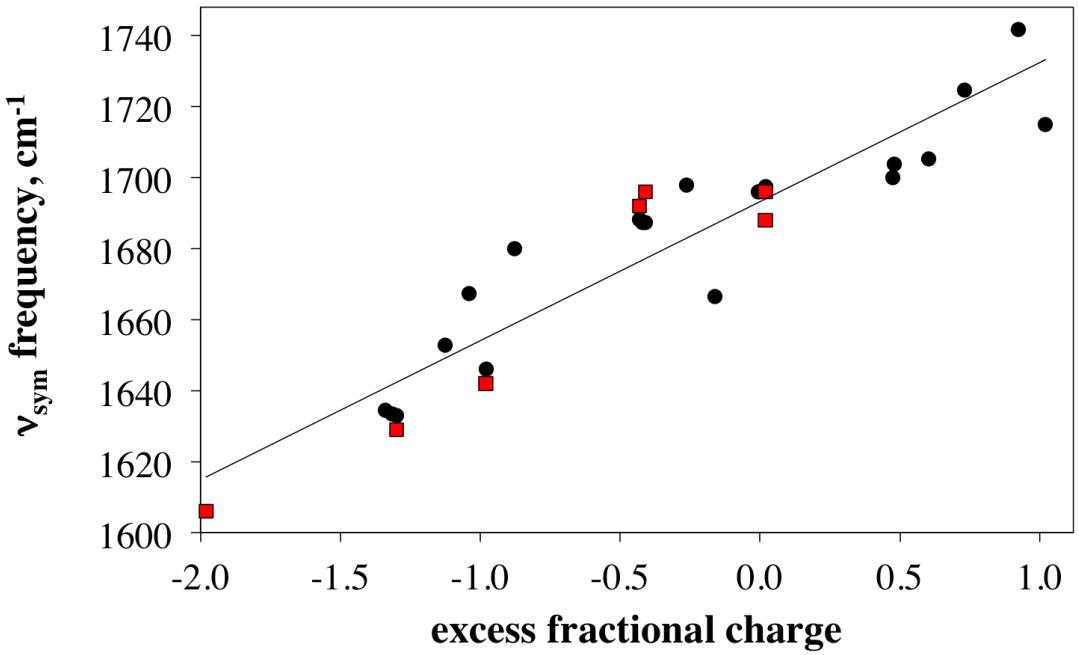

Figure 4.6. Calculated (black circles) and experimental (red squares) ν_{sym} frequencies as a function of the excess fractional charge on the perylene core as determined by population analysis.

Figure 4.6 shows the resulting dependence of ν_{sym} on the excess fractional charge on the perylene core. Experimental values for the imide stretching frequency for a few of the molecules were found in the literature and are overlaid as red squares showing good agreement with the calculations. A linear regression of the DFT calculated frequencies and the experimental values from the literature indicates that the ν_{sym} shifts by 39.2 cm^{-1} per charge. This provides a calibration curve that can be used to map the measured frequency shifts onto a fractional charge coordinate for the PTCDI OFETs monitored by VSFG.

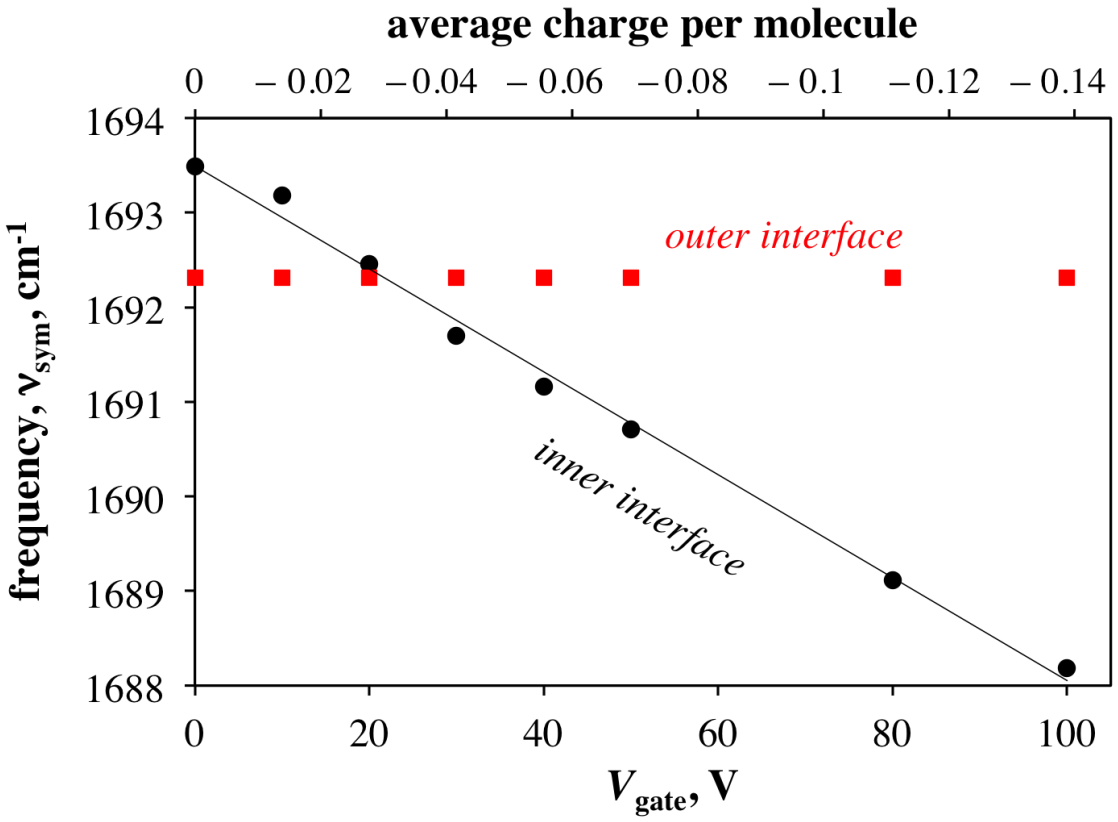

Figure 4.7. Best fit parameters for the inner (black circles) and outer (red squares) interfacial imide symmetric stretching frequencies as a function of applied gate bias and the calculated charge per PTCDI molecule at the buried interface.

Figure 4.7 shows the frequencies of ν_{sym} at the inner and outer PTCDI interfaces as the OFET is biased to accumulate electrons. Using the results of the calculations above, we can plot these same numbers onto the fractional charge coordinate (top x-axis). Based on the capacitance of our devices, we expect 7.4×10^{12} injected charges per cm^2 at 100 V. If these electrons were fully delocalized over the areal density of PTCDI (2.3×10^{14} molecules per cm^2),[117, 133-134] our calibration curve would predict a frequency shift of only 1.3 cm^{-1}, yet we measure a 5.3 cm^{-1} shift. Clearly the injected charges are *not* fully delocalized over all PTCDI molecules at the interface. We must conclude that this buried interface vibrational peak must encompass neutral and partially charged populations. We cannot resolve the two populations with our current instrumentation, but the combination of measurements and calculations in Figure 4.7 indicate that there are 0.14*e* per PTCDI at V_{gate} = 100 V; electrons are delocalized over seven PTCDI molecules on average. Assuming equal oscillator strength for the charged and neutral species, we view this as an upper limit and conclude that the electrons are probably localized to fewer than seven molecules in this material.

4.4: Conclusions

The complexity that arises in spectroscopy of samples with multiple interfaces can make data interpretation feel like an exercise in futility. In this chapter, I have shown that optical interference, often considered a nuisance, can actually be a true ally when properly modeled. As long as the optical characteristics of the layered materials are known (or measured), the transfer matrix formalism provides a straightforward pathway to a more complete and accurate treatment of VSFG observables that avoids unnecessary and erroneous approximations. The data analysis herein showed that the vibrational frequencies at the buried interface of an OFET shift by only a few wavenumbers due to charges being delocalized over about seven molecules or less.

The magnitude of this shift would likely be overlooked with most modern VSFG instruments or its effect misinterpreted by single interface interpretations. As organic electronic materials improve and charges become even more delocalized, such spectroscopic handles will become increasingly difficult to monitor. Leveraging the interference between multiple VSFG signals is one way to achieve the requisite sensitivity to small frequency shifts and lineshape changes.

Chapter 5: Frequency Comb SFG: A New Approach to Multiplex Detection

5.1: Introduction

As stated in previous chapters, vibrational sum frequency generation (VSFG) spectroscopy is a surface-specific technique that is important for the characterization of material interfaces.[70-71, 73, 88-89, 94, 96-97, 99-100, 135] In these measurements, sampling multiple components of the second order susceptibility tensor, $\chi^{(2)}$, enables orientational information to be obtained.

In practice, obtaining absolute molecular parameters is rarely achieved, in part because the local field corrections due to beam geometries and optical coefficients are not applied because they are not known. In addition, orientation distributions of the transition dipoles can have a profound influence on the determined quantities, sometimes to the point of obscuring them altogether when wide distributions are present at the interface.[136] Furthermore, for absolute orientation to be determined, the signal phase is required, which is only obtained in heterodyne detected experiments.[89-90, 137] Nonetheless, VSFG excels at providing semi-quantitative orientation information about interfacial environments and has been used to determine order and orientation in small molecule and polymeric semiconducting organic thin films,[59-60, 64, 135, 138-139] at aqueous interfaces,[88-89, 92, 140] and in self assembled monolayers.[69, 140-142]

Orientational studies require more than one of the nonzero $\chi^{(2)}$ tensor elements to be sampled. This is typically achieved by performing separate experiments in which different polarization combinations are used. Building on the work of Smits and

coworkers, we previously reported a method of collecting all four VSFG polarizations at once.[143-145] The utility of this approach was highlighted by a study in which we monitored interfacial ordering and orientation in real-time while thermally annealing an organic thin film.[59] However, a challenge in that work was that it required simultaneous alignment of three pump beams onto the sample and four signal beams onto the detector. Since the visible pump beams were aligned to the sample at different incident angles, the coefficients for reflection and the phase matching directions were slightly different, introducing new sources of error in the measurements.[143] The generated signal beams that contained a mixture of polarizations (to be later separated by a birefringent optic) also needed to be independently steered to the entrance slit on the monochromator.

In this chapter, I present a new method for multiplex polarization data collection. By using a modified 4f pulse shaper, a simple frequency comb is generated that can then be used as the upconverting beam with a broadband IR source in a VSFG experiment. This method has improvements over the previous approach, including collinear alignment and independent tailoring of pulse timing, bandwidth, and polarization within the visible beam frequency comb. This ultimately allows for faster data collection with ease of alignment and improved data fidelity for samples that change on the time scale of a measurement and/or are spatially heterogeneous.

5.2: Experimental Setup and Measurement Procedure

Laser Setup

The details of the femtosecond laser setup and mIR generation are detailed in Chapter 3. The visible frequency comb was created by amplitude-shaping 500 mW of the uncompressed output from the regenerative amplifier (prior to the compressor) in a modified 4f pulse shaper, as shown in Figure 5.1. A typical 4f pulse shaper consists of a

diffraction grating placed at the focal point of a double convex lens and slit with a mirror behind it at the other focal point.[146-147] The incoming light is dispersed horizontally by the diffraction grating and is imaged to a stripe at the retroreflector. The slit selects a portion of the input bandwidth to be reflected back through the lens, recombined at the diffraction grating, and reflected out of the shaper (typically at a slightly different height). The modified 4f shaper in Figure 5.1 introduces a D-shaped broadband dielectric mirror after the refocusing lens, sending approximately half of the dispersed light to a second slit and mirror at the focal point of the lens. Retroreflections from both mirrors in the pulse shaper recombined at the diffraction grating to a single beam that consisted of two narrowband pulses (approximately 1 nm FWHM) that were collinear but separated in wavelength by about 15 nm. Owing to the uncompressed nature of the input 800 nm light, the two collinear pulses were also dispersed in time by tens of ps. This setup allowed individual control of the bandwidths of the two frequency comb “teeth”. The retroreflector and slit pairs were on translation stages to optimize the selected frequencies and the retroreflector positions relative to the focal plane of the lens. For our purposes the comb was shaped as shown in Figure 5.1 with two spectral peaks at 790 and 806 nm. An alternative approach would be to use a double slit at a single mirror rather than dividing the beam into two arms of the shaper. This would simplify alignment but might offer less flexibility in tailoring the bandwidths of the spectral teeth. We also note that the arrangement in Figure 5.1 enables one to independently adjust the focal properties of the two beams to give different focal spot sizes.

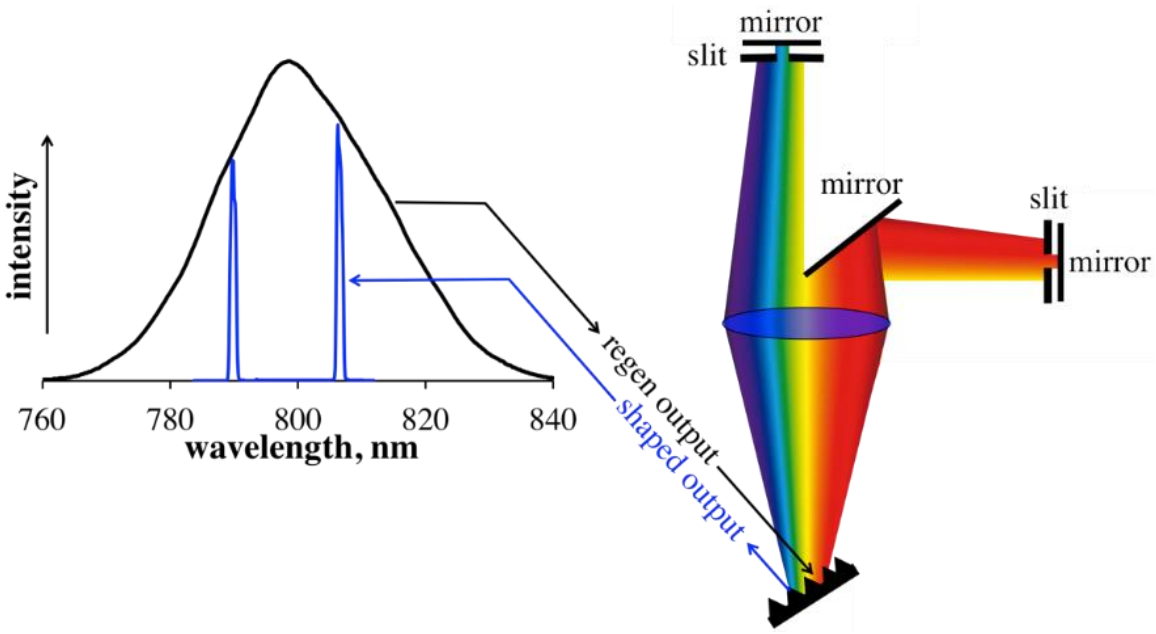

Figure 5.1: Right: Diagram of the modified 4f pulseshaper to produce a simple frequency comb showing the relative positions of the diffraction grating, lens, mirrors, and slits. The mirror after the lens directs half of the light to a second slit that is retroreflected back and recombined at the grating with the shaped throughput from the other slit. Left: The input and output spectrum of the modified pulse shaper.

For VSFG to occur, both the visible and mid-IR pulses need to be overlapped in space and time at the sample. Given the uncompressed nature of the 800 nm broadband light entering the pulse shaper, the two narrowband pulses needed to be retimed to arrive at the sample at the same time. This was achieved with a simple retiming section constructed from two sharp cut-on dichroic beamsplitters that reflected the short wavelength pulse and transmitted the long wavelength pulse (Semrock, 785 nm BrightLine®), as shown in Figure 5.2. The dichroic beamsplitters went from 5% to 95% transmission over 5 nm with a 50% transmission at about 798 nm. The two legs of the retiming section enabled adjustment of the arrival times of the two visible pulses at

the sample as well as independent beam steering to optimize their collinearity as they continued on to the sample. Before recombining at the second dichroic beamsplitter, the shorter wavelength beam transmitted through a half waveplate and thin film polarizer to independently control its polarization from the longer wavelength beam. Both beams were then recombined at the second beamsplitter and aligned as a single beam to the sample.

The visible and IR beams were focused at the sample using a 60° off-axis parabolic reflector and the emitted VSFG signal was collected and collimated by a matching parabolic reflector. The emitted signal was directed through a twisted periscope and through a lowpass filter to remove the visible pump. It was then focused onto the slit of a 150 mm monochromator with a 15 micron slit size followed by detection with a liquid N_2 cooled CCD camera (Princeton Instruments). In a typical alignment procedure, the visible and IR beams were overlapped in space at the sample stage in a ZnS crystal, which produced an extremely large nonresonant VSFG signal for initial alignment and timing. The delay stages for the IR and one of visible delay stages in the retiming section (Figure 5.2) were used to maximize signal. After this, these two IR and visible stages were not moved again and the delay stage of the other visible beam was used to maximize its VSFG signal through the monochromator. After finding the correct timing of the pulses, the sample was switched to a 100 nm thin film of ZnO deposited by atomic layer deposition on a Si wafer. This sample gave significant amounts of VSFG due to its lack of centrosymmetry through the bulk of ZnO, but from a thin slab so that fine adjustments could be made to the sample position, beam pointing, and timing to further optimize the signal before switching to the organic thin films of interest. A HeNe laser was used to optimize sample positioning as described previously.[65-66]

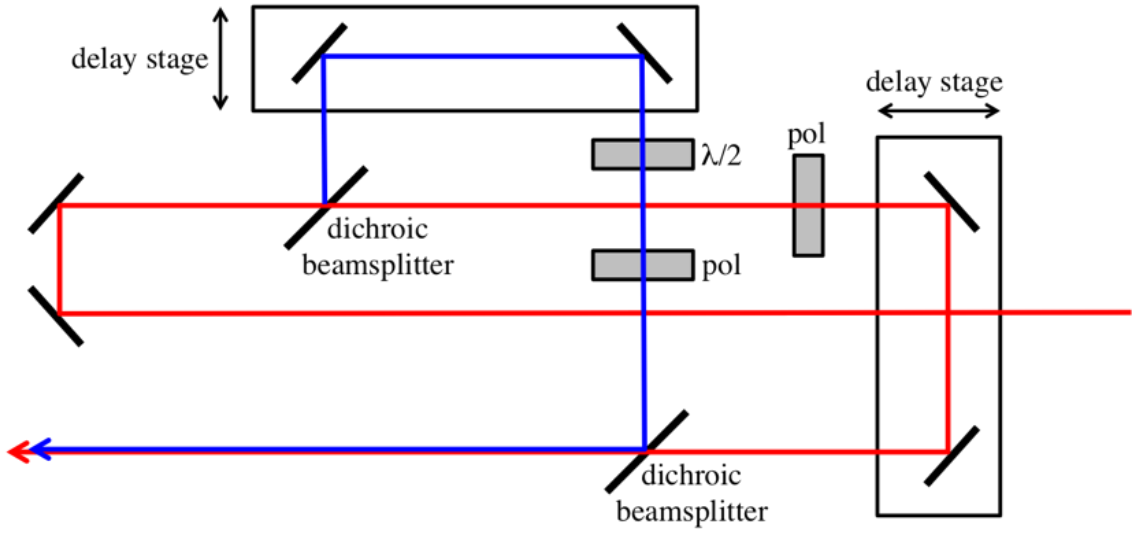

Figure 5.2: Diagram of the retiming portion of the visible beam path. The frequency comb 'teeth' are separated by a dichroic beamsplitter for independent timing, pointing, and polarization control. The 790 nm beam polarization is controlled by a halfwave plate and a thin film polarizer. The 806 nm polarization is cleaned up by a Glan-Thompson polarizer.

Thin films of α–sexithiophene (6T, 35 nm) and dioctyl-perylenetetracarboxy-diimide (PTCDI, 100 nm) were prepared by vapor deposition onto RCA-cleaned glass and thermal oxide SiO_2 wafers, respectively, using a homebuilt organic vapor deposition chamber.[58] For VSFG measurements on organic thin films, two exposures were collected first with both IR and visible beams and second with the IR blocked to subtract out the background. Five spectra were collected with 5 and 3 minute exposure times for 6T and PTCDI films, respectively, followed by averaging. Cosmic rays were corrected by a program that automatically identified a cosmic ray and compared pixels of the same wavelength in the other exposures. A reference spectrum was collected on ZnO using a ppp polarization combination for both visible beams. Further details of data analysis are described in the discussion below.

5.3: Results and Discussion

Figure 5.3a shows the reference spectrum collected in ppp from ZnO using the frequency comb upconverting beam. Two wide, approximately Gaussian peaks are observed at 706 and at 721 nm, each with 150 cm^{-1} bandwidth to match the bandwidth of the IR beam. These are nonresonant VSFG signals generated by the 790 and 806 nm visible beams, respectively. The peaks are slightly misshapen by water vapor absorption of the IR beam, which is tuned here to approximately 1450 cm^{-1}. The spectra are similar in shape and intensity. Subtle differences in intensity are due to errors in coalignment of the two visible pulse in the frequency comb leading to very slight differences in signal phase matching and alignment to the monochromator slit. This is not overly important as the subsequent sample spectra will be divided by this reference spectrum and will inherit the same pointing differences to compensate for any systematic inconsistencies. Similarly, the diffraction grating in the monochromator has small differences in efficiency at these two wavelengths (<5%), but this will also be normalized in the sample spectra when dividing by the reference spectra shown here. The shorter wavelength VSFG peak is marginally broader than the longer wavelength peak. This is because the spectral resolution is lower at shorter wavelengths – a larger energy range falls on each pixel at shorter wavelengths, which will become more apparent in the resonant VSFG spectra discussed below.

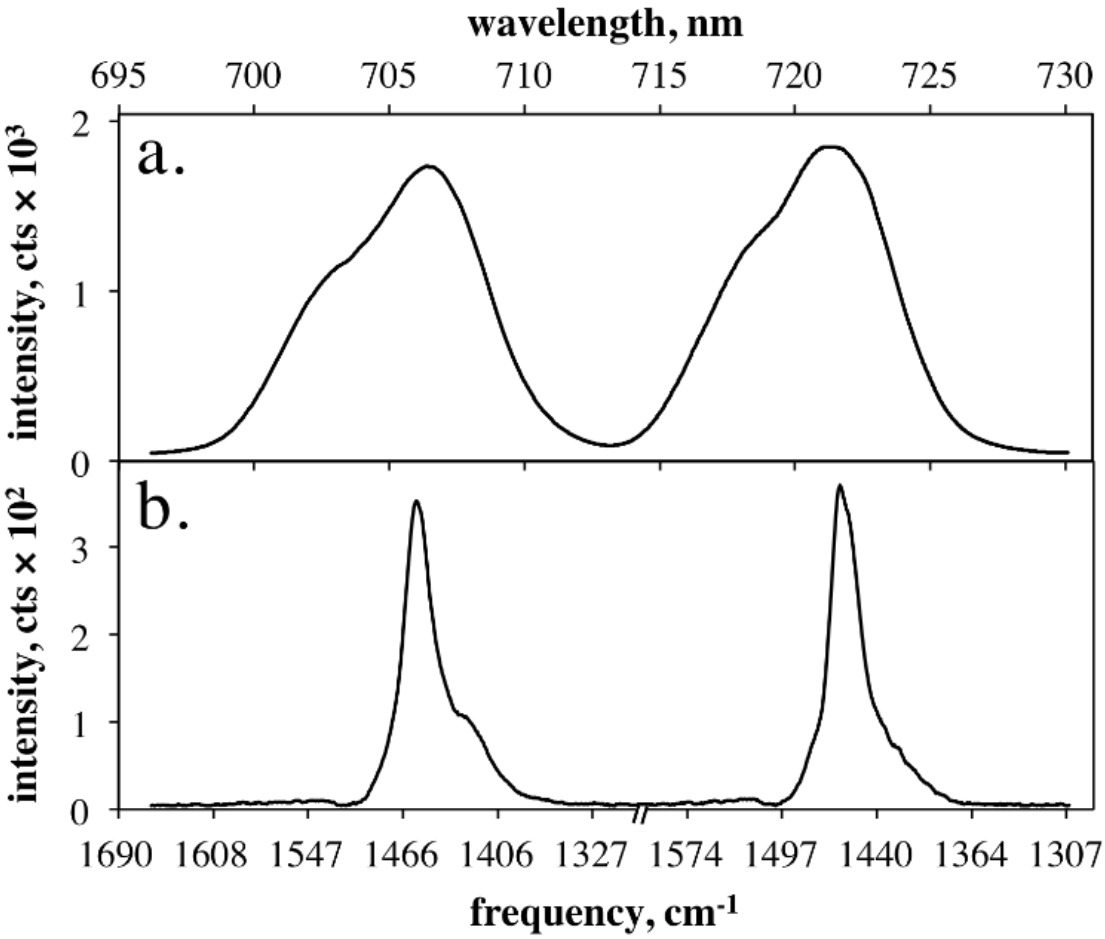

Figure 5.3: a) VSFG spectrum of ZnO thin film and b) a 6T thin film, both collected with the ppp polarization combination. The bottom frequency axis has been created by down converting the summed frequencies with the known center wavelengths of the frequency comb teeth.

Figure 5.3b shows the VSFG spectrum generated from a 35 nm thin film of 6T on glass using the ppp polarization combination. The lower axis shows the down-converted frequency ranges using the measured upconverting visible beam spectra, but we emphasize that this figure shows a single continuous spectrum collected from the sample using the same IR beam and the frequency comb beam to upconvert two spectrally separated VSFG regions. The two spectra are identical within our signal-to-noise level, and have relative intensities that match those of the reference spectrum in

Figure 3a. These demonstrate multiplex VSFG data collection from the same sample spot in a single spectrum using the spectral resolution imparted by a frequency comb rather than vertical displacement into separate spectra.

A more interesting case is shown in Figure 5.4 in which we apply this approach to a 100 nm film of PTCDI, a material that we have shown to have a markedly different VSFG response in different polarization combinations.[65] For this experiment, we rotated the polarization of the short wavelength part of the comb to be s-polarized, while setting the IR beam to a mixed polarization. From previous work with this system, we expected that the ssp VSFG spectrum would be over an order of magnitude more intense than the sps combination.[65] Since a single integration time was used to collect the multiplex spectrum, the IR beam was rotated to put 3% of the power into the p-polarization and 97% in the s-polarization so that the signal-to-noise ratio would be the same for the two regions. The spectrum in Figure 4a is a single spectrum with the low and high wavelength portions color coded to indicate that these regions were upconverted with a different part of the comb. The low wavelength region shows the raw ssp VSFG spectrum; the high wavelength region shows the sps VSFG spectrum. A ppp reference spectrum was collected (not shown) with the IR tuned to the 1680 cm^{-1} region, and was used to normalize the ssp and sps spectra, resulting in the spectra in Figure 4c (with consistent color coding). The normalization process accounts for the differences in intensity across the IR bandwidth, and the spectral features are accordingly reshaped. The resulting spectra are identical to those previously reported but were collected in half the time.[65]

Interestingly, this optical design actually generates all four VSFG polarization combinations at once (ppp, ssp, sps, and pss). Before entering the monochromator the analyzing polarizer removes the ppp and pss signals and transmits the ssp and sps.

The ssp and sps combinations give different information and their comparison allows one to determine the orientation of the IR transition dipole for a particular resonance.[73] In a previous report, we demonstrated how film thickness could be used to favor the VSFG signal from the buried interface of a thin film, and we showed that ssp and sps were the only polarization combinations that could be paired together to favor the buried interface for the same beam angles and film thickness.[65, 75] In this context, the current results are unique in their ability to provide this particular pair of VSFG signals simultaneously. Previous reports have always differentiated multiplexed signals by the analyzer polarization, forcing pairs of ppp/sps or ssp/pss using mixed polarization IR, or ppp/ssp or sps/pss using mixed polarization visible.[143-144] Here we use a single analyzer polarization with mixed IR polarization *and* mixed visible polarization, but separate the signals with the monochromator rather than a birefringent beam displacer after the sample.

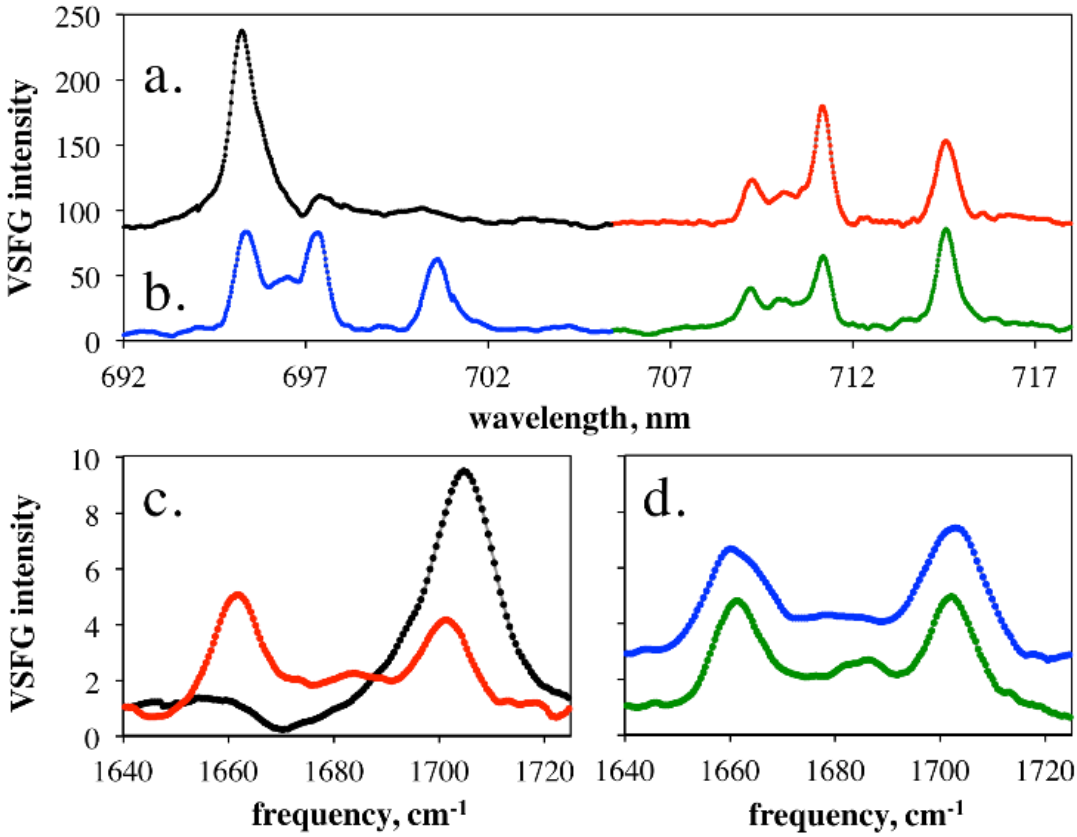

Figure 5.4: a) VSFG spectra of a PTCDI thin film collected in ssp (black) and sps (red), and b) using sps (blue) and sps (green) polarizations. c) ssp and sps (from part a) and d) sps and sps (from part b) after normalization by the ppp reference spectrum.

To demonstrate the immunity of this beam arrangement to misalignment, Figure 5.4b shows the VSFG spectrum for the same PTCDI sample but with both visible pulses in the frequency comb rotated to p-polarization and the IR returned to full s-polarization. In this case, the longer wavelength comb was slightly misaligned onto the sample leading to a pointing error in the generated signal. As a result, the relative peak ratios between the short and long wavelength regions are not the same. However, the ppp reference spectrum also shares this misalignment and can be easily used to correct the data assuming no beam adjustments were made between the reference and sample spectra. Figure 5.4d shows that once they are divided by the ZnO ppp reference

spectrum the data appear to be nearly identical. We believe that the pointing sensitivity is the result of spatial chirp in the IR beam at the sample, which would cause a difference in the frequencies mixed at the interface that give rise to the VSFG signal. However, the fact that normalizing by the ZnO reference spectrum corrects this shows the considerable resilience of this technique.

5.4: Conclusions and Future Directions

In conclusion, we have demonstrated for the first time that a simple frequency comb can be used for VSFG, and that the spectral resolution of the resulting signals opens the door to a new, simpler approach to multiplex polarization measurements. This system allows for collection of the ssp and sps polarization combinations (and, in principle, pss and ppp) from the same spot, at the same time, and with the same incident angles in a reliable and robust way. Generally speaking, this is an improvement over other traditional VSFG approaches as it reduces problems with multiple beam alignments at the sample and at the detector, sample heterogeneity, and changes in laser power, while enabling one to collect data faster. Compared to our previous multiplex detection scheme, this one allows the simultaneous collection of ssp and sps from the same spot with the same incident angle, a combination that shows a greater affinity for the buried interface in layered systems.

In addition to the practical improvements of the frequency comb approach, a number of additional directions could be explored. To begin with, one might design a double (or triple or quadruple) slit using a single retroreflector in the 4f pulse shaper to simplify its alignment. Furthermore, one could envision replacing the dual slit 4f pulse shaper with a single optic such as an etalon in the mode of Lagutchev and coworkers.[148] For example, a simple calculation shows that an air etalon can be designed for the 800 nm central wavelength using 83% reflective mirrors with a separation of 22.5 microns

(6.66 THz free spectral range) to give two narrow Lorentzian peaks at 790 and 804 nm. This single optic could replace the entire shaper portion of our design, but at the expense of control over the spectral width of the teeth of the frequency comb. With enough bandwidth from the amplifier, one might also modify the pulse shaper (or design an etalon) to give three or four peaks in the frequency comb. This would require three dichroic beamsplitter retiming stages in order to obtain the requisite timing control over all four beams, but when combined with mixed polarization IR would give all four VSFG polarization combinations simultaneously in a single spectrum. We reiterate that even without the additional teeth, our current arrangement generates all four polarization combinations, and the other two (pss and ppp) are readily obtained by analyzing for the p-polarized VSFG signal. The independent timing of the two legs opens new directions as well. Changing timing allows for the mistiming of one leg to look at data simultaneously with and without nonresonant signal suppression.[148] Also, independent control of the slit of either leg allows for data collection with different spectral resolutions, perhaps in cases where signal may be very low and full resolution is not needed in one polarization. And finally, replacing the half waveplate with a quarter waveplate would enable experiments in which one beam is circularly polarized while the other is linearly polarized to explore chiral VSFG signals.

Chapter 6: Interfacial Spectra of PTCDI-C8 on Al_2O_3

6.1: Introduction

In this study, the effect of an aluminum oxide (Al_2O_3) dielectric on the interfacial vibrational spectrum collected by VSFG will be examined. As discussed earlier, a thin film interference model described in Chapter 2 can be used to assess unambiguously signal from the buried dielectric semiconductor interface that is convoluted with the outer interface signal. As emphasized in Chapter 1, the dielectric semiconductor interface in organic field effect transistors is of major importance. The charge conduction that occurs in the OFET device happens at this interface. Molecular packing and the degree of π-π stacking of the molecules that make up the material are influential in how the device works. Furthermore, the nature of the dielectric influences OFET performance due to its roughness, surface energy, and chemistry. [44-50] Also, the dielectric can be modified further by self-assembled monolayers (SAMs), from passivation of charge traps, and smoothing out of dielectric, to affecting interfacial dipoles and molecular orientation. [45, 48-49, 117, 149] SAMs have also been shown to make typically non-air stable semiconductors air stable.[150]

Thinner dielectric layers lead to lower threshold voltages in devices, lowering power consumption.[151] However the traditional dielectric of choice SiO_2 has high defect rates at very thin dielectric thickness and leakage current is high. To surmount this problem other dielectrics have been examined. Al_2O_3, with a dielectric constant of 9 compared to SiO_2 at 3.9, offers a way to increase device performance.[151] It provides

higher capacitance for a given thickness when compared to SiO_2, and ALD deposition allows for thin conformal and defect free layers to be deposited.[151-154]

Unfortunately, it is found that bare Al_2O_3 dielectric leads to lower charge carrier mobilities when compared to SiO_2 in P3HT based devices but proper SAM functionalization can eliminate this effect.[155] Veres and coworkers found this effect for a range of semiconducting materials and attributed it to an increase in local energetic disorder of the semiconductor when placed on higher k dielectrics. The more polarizable higher k dielectrics contain more randomly ordered dipoles in the dielectric than lower k dielectrics which interact with the semiconductor.[156]

In this study, two different thicknesses of PTCDI-C8 were examined by VSFG spectroscopy on a single thickness of thermally grown SiO_2, and a range of thicknesses of ALD Al_2O_3. Different thicknesses of both the semiconductor and the dielectric were used to constrain the multilayer interference fitting routine that fits several spectra simultaneously keeping some variables independent and others not.

6.2: Experimental

Sample Preparation

PTCDI-C8 was used as received (Sigma-Aldrich) without further purification. It was deposited by physical vapor deposition in either 20 nm or 200 nm films onto thermally grown SiO_2 (300 nm thickness) on Si wafers (University Wafer), or onto Al_2O_3 grown by atomic layer deposition (ALD) on Si wafers. The deposition involved a home built physical vapor deposition chamber that heats the PTCDI in a crucible under high vacuum, approximately 6.0×10^{-6} torr. The sample was held above the crucible and material deposited upon it. Deposition rate and thickness was tracked via a quartz

crystal microbalance and corroborated via spectral ellipsometry (VASE, J. A. Wollam Co., Inc.)

The SiO_2 dielectrics were cleaned before being used via the RCA 1 and 2 method, involving soaking in an 80 °C solution of water, H_2O_2 and ammonium hydroxide in a 5:1:1 ratio for 5 minutes, followed by soaking in a solution of HCl for 5 minutes.[58] The Al_2O_3 layers were deposited in 3 different thickness via ALD using Trimethylaluminum and water as precursors. The substrates were kept at 350 °C. The deposition rate is very reproducible and layers conformal. Thicknesses of 10 nm, 65 nm, and 95 nm of Al_2O_3 were deposited. The Al_2O_3 was not cleaned in any way after this step.

Data Collection

The details of the experimental setup have been described in Chapter 3. Briefly, spectra were integrated from 3 to 10 minutes depending on signal strength and multiple polarization combinations taken simultaneously using the frequency comb described in Chapter 5. Atomic force microscopy (AFM) was performed on 20 nm samples of PTCDI on Al_2O_3 and SiO_2 using AC mode in open loop mode (Agilent 5500).

Global Fittting

The data were fit to a model that calculates and models thin film interference effects on the observed VSFG signal, as described in Chapter 2.[65, 75] The intensity is the absolute value squared of the second order response $\chi^{(2),}$ and the transfer integral T:

$$I_0^{ijk} = \left|\chi_{NR} + \sum_v^2 T_v^{xyz} \chi_v^{xyz}\right|^2 \quad [6.1]$$

The model is the sum of a transfer integral and second order signal from interface *v*=1, the air/PTCDI interface, and *v*=2 the PTCDI/dielectric interface.

The second order response is itself broken up into several parts that interfere with each other at the electric field level. There is a non-resonant contribution that is modeled to originate at no particular interface:

$$\chi_{NR} = Ae^{i\varphi} \quad [6.2]$$

Each interface, *v*=1 or *v*=2, was modeled as having two resonant contributions to the second order response modeled as Lorentzians, one each for the asymmetric and symmetric imide stretch for both interfaces.

$$\chi_{\upsilon}^{ijk} = \frac{A_{\upsilon}^{ijk}}{(\omega_{res} - \omega - i\Gamma)} \quad [6.3]$$

Modeling the Transfer integral

Table 6.1: The PTCDI thicknesses and dielectric thicknesses that were globally fit.

	20 nm PTCDI	200 nm PTCDI
300 nm SiO_2	NONE	SSP,PPP
95 nm Al_2O_3	SSP	SSP,PPP
65 nm Al_2O_3	SSP	SSP,PPP
10 nm Al_2O_3	NONE	SSP,PPP

In the fitting procedure the transfer integral for the outer interface was kept the same for samples regardless of the dielectric in use. The transfer integrals consisted of frequency dependent refractive indices that are expressly known for air, PTCDI, SiO_2, and Si for the frequencies studied. However, for the Al_2O_3 films, refractive indices were

estimated for each of the important frequency window, mid IR and visible, and taken to be constant for the range of frequencies needed in the experiment.[157-159]

Each T was independently calculated and the nonlinear response was determined from the fit. All 10 spectra that were fit were fit simultaneously, with some values being shared between spectra. In the case of the non-resonant response, the intensity and phase could float independently for every sample at every polarization combination. This was deemed to be a valid choice as each sample for each polarization combination had a unique combination of PTCDI and semiconductor thickness and it is assumed that some non-resonant signal is coming from both materials.

Modeling the resonant portion of the nonlinear response was done as a series of complex Lorentzians. Each apparent resonant signal in the spectra was assigned two Lorentzians for the asymmetric and symmetric imide stretches. Assigning the frequencies of the Lorentzians: the outer facing peak centers could float but were kept the same for every polarization data set on every sample. The buried, semiconductor/dielectric, frequencieswere kept the same for every experiment involving the same dielectric; every polarization experiment on SiO_2 regardless of PTCDI thickness had the same buried interface frequencies and likewise for the Al_2O_3 experiments. For the line widths of the Lorentzians, Γ, all asymmetric stretches were given one value allowed to float, likewise for the symmetric Γ. The amplitudes of the resonances were kept independent between the different polarization combinations and between interface environments. While data were collected for all semiconductor (200 nm and 20 nm) and dielectric (200 nm SiO_2 and 10, 65, and 95 nm) thicknesses for three polarization combination experiments (PPP, SSP, SPS) not all were able to be included in the fit (see Table 6.1).

6.3 Results and Discussion

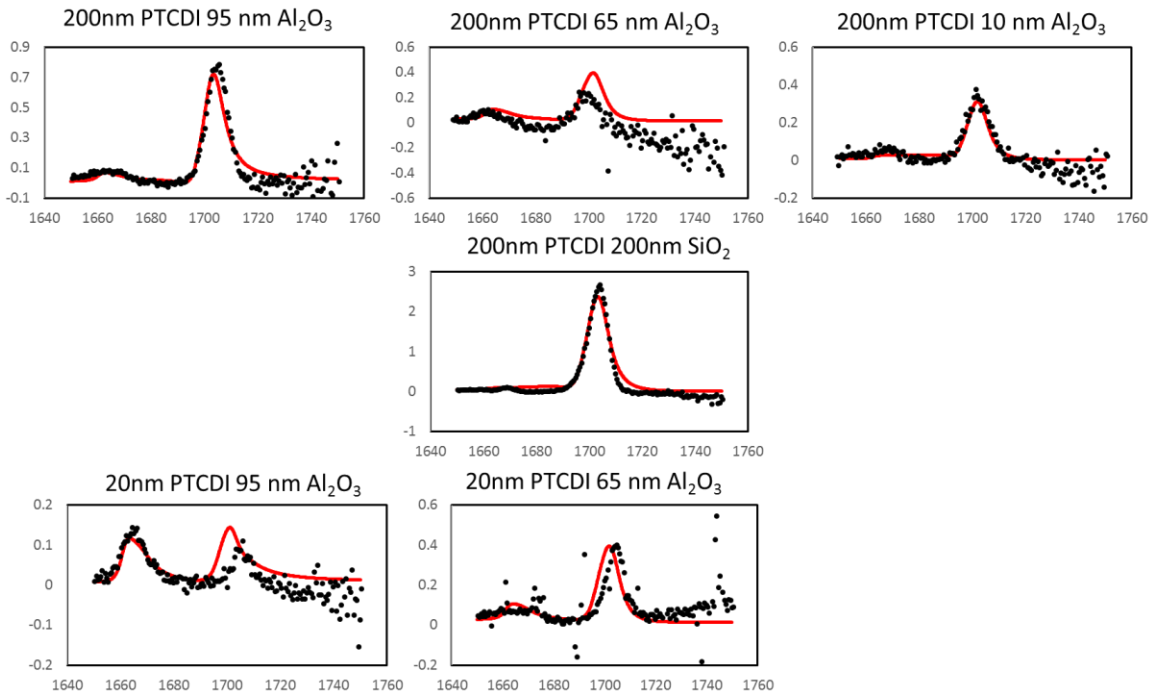

Figure 6.1: Normalized SSP data (black dots) overlaid with results of simultaneous fit (red line) for all the fitted PTCDI and dielectric combinations.

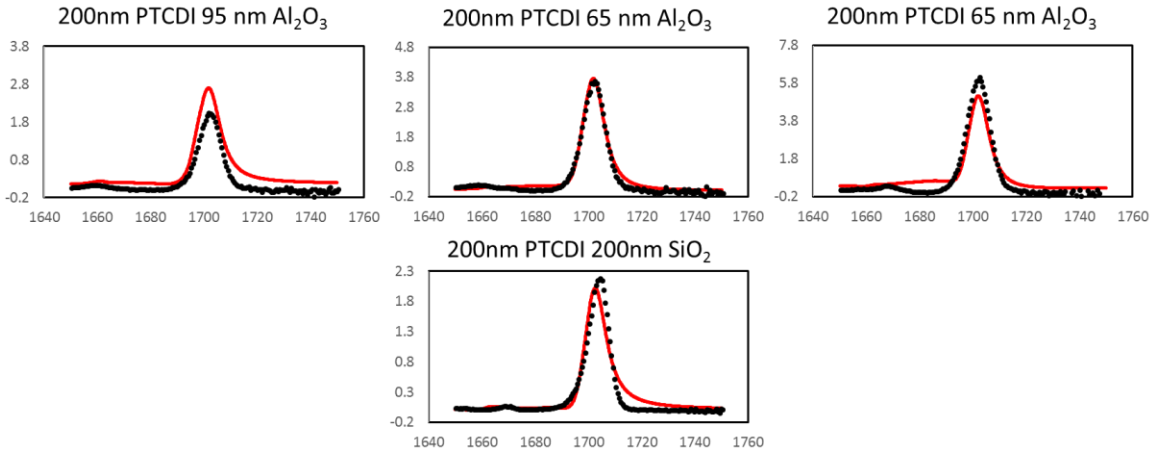

Figure 6.2: Normalized PPP data (black dots) overlaid with results of simultaneous fit (red line) for all the fitted PTCDI and dielectric combinations.

Figures 6.1 and 6.2 show the spectra that were fit using the above-mentioned model. As shown in the table, no SPS data were fit as the signals had very low signal to noise. The fits are in generally good agreement with the data, especially considering how many variables were shared between them. Looking first at the SSP data, the fits for most of the spectra capture the correct resonant frequency of the symmetric stretch and background, except on the lower intensity spectra. Also, the asymmetric stretch, while included in the model, typically was not captured very well as it at times is also very low intensity. In the SSP spectra, one interesting effect captured by the model is that for the 20 nm of PTCDI on 95 nm of Al_2O_3 the asymmetric mode is on par in magnitude with the symmetric stretching mode a reversal of trends generally seen in PTCDI.[65, 75]

Looking at the PPP data, the fits are generally acceptable, the intensities are around the same as they appear in the data and the peaks show up at the right frequency. At times the line widths are not accurate, especially in the thickest PTCDI samples on the SiO_2, but that may be due to forcing all spectra to share the same line width in the fit.

Given the error in the fits, the sources of the inherent error will now be discussed. VSFG spectra can be very sensitive to the angle of incidence of the incoming laser beams and to the thicknesses of the material layers in the sample.[76] While the thicknesses reported above are roughly correct, small changes could introduce new error in the fitted parameters. Also, for the Al_2O_3 transfer product, constant values were used in the frequency range of interest. This is a good assumption as for the relevant frequencies the refractive index is largely flat. If this were a source of error, it is conceivable that the Al_2O_3 data might be worse fit, but any evidence of this could also likely be the signal to noise. Another possibility is error in the transfer product of the

PTCDI itself. PTCDI's refractive index changes greatly in the range of frequencies used for this experiment, indeed we are seeing resonant peaks after all. We have seen in the data collected on PTCDI shifts in our assignment of the resonances due likely to uncertainty in the frequencies assigned by the monochromator, as much as several wavenumbers. However, the corresponding dips or changes in the nonlinear refractive index are stationary. This would cause error in the fitted parameters as well.

Given all this, however, it is stressed that these fits are quite good. Relatively few parameters were used to fit these 10 spectra, and all changes were modeled solely due to changes in thickness either of the dielectric or the semiconductor. In fact, we can see that most the observed changes are due simply to those changes in the layer thicknesses.

Fitting Results

Table 6.2: Nonresonant amplitude results for the fitted PTCDI and dielectric combinations

PPP Non-Resonant Amplitude 200nm PTCDI	
95nm Al_2O_3	0.161
65nm Al_2O_3	0.0252
10nm Al_2O_3	0.200
200nm SiO_2	0.007

SSP Non-Resonant Amplitude 200nm PTCDI	
95nm Al_2O_3	0.0123
65nm Al_2O_3	0.015
10nm Al_2O_3	0.006
200nm SiO_2	0.021
20nm PTCDI	
95nm Al_2O_3	0.006
65nm Al_2O_3	0.013

Looking at Table 6.2 the non-resonant amplitudes are given for all the fitted spectra. It was expected that since Al_2O_3 has been observed to have such a large non-resonant second order response that as the Al_2O_3 thickness was increased there would

be a corresponding increase in the response. However, this is not the case. Looking across all data, it does not appear that the data correlate with any thickness increase, dielectric or semiconductor.

Table 6.3: Resonant results of the simultaneous fit, frequency, amplitude and Γ for PTCDI on Al_2O_3 and SiO_2 for SSP and PPP polarization combinations

Symmetric Stretch PPP

	Frequency (cm^{-1})		Amplitude		Γ (cm^{-1})
	outer	inner	outer	inner	
Al_2O_3	1703.4	1703.94	1.340×10^{-3}	1.402×10^{-9}	7.477
SiO_2		1704.97		2.207×10^{-4}	

Asymmetric Stretch PPP

	Frequency(cm^{-1})		Amplitude		Γ (cm^{-1})
	outer	inner	outer	inner	
Al_2O_3	1668.94	1666.15	5.194×10^{-5}	5.622×10^{-8}	5.854
SiO_2		1665.94		3.201×10^{-4}	

Symmetric Stretch SSP

	Frequency (cm^{-1})		amplitude		Γ (cm^{-1})
	outer	inner	outer	inner	
Al_2O_3	1703.4	1703.94	8.541×10^{-4}	7.852×10^{-4}	7.477
SiO_2		1704.97		3.841×10^{-3}	

Asymmetric Stretch SSP

	Frequency (cm^{-1})		amplitude		Γ (cm^{-1})
	outer	inner	outer	inner	
Al_2O_3	1668.94	1666.15	7.396×10^{-9}	2.730×10^{-4}	5.854
SiO_2		1665.94		9.061×10^{-5}	

Table 6.3 shows the results of the simultaneous fits for both the symmetric and asymmetric imide stretches. While the asymmetric was fit, its signal to noise was too low to get precise information out of it.

There remains however, a plethora of information in the symmetric stretch. Γ was taken to be the same for every symmetric stretch and fit to the data simultaneously. Given the fact that our VSFG line width is heavily influenced by the visible pulse linewidth this is a reasonable assumption. The frequencies were kept tied together regardless of polarization but different for chemical environment. The outer imide frequency was 1703.4 cm^{-1} and the buried mode was 1704.97 cm^{-1} for SiO_2 and 1703.94 cm^{-1} for Al_2O_3. This is roughly consistent with previous studies that found the buried frequency is slightly red of the outer interface or very close to it for SiO_2 surfaces.[58, 65, 160]

The similarity of the SiO_2 and Al_2O_3 frequencies are also understandable since both surfaces are likely hydrated hydrophilic environments to the PTCDI molecules.

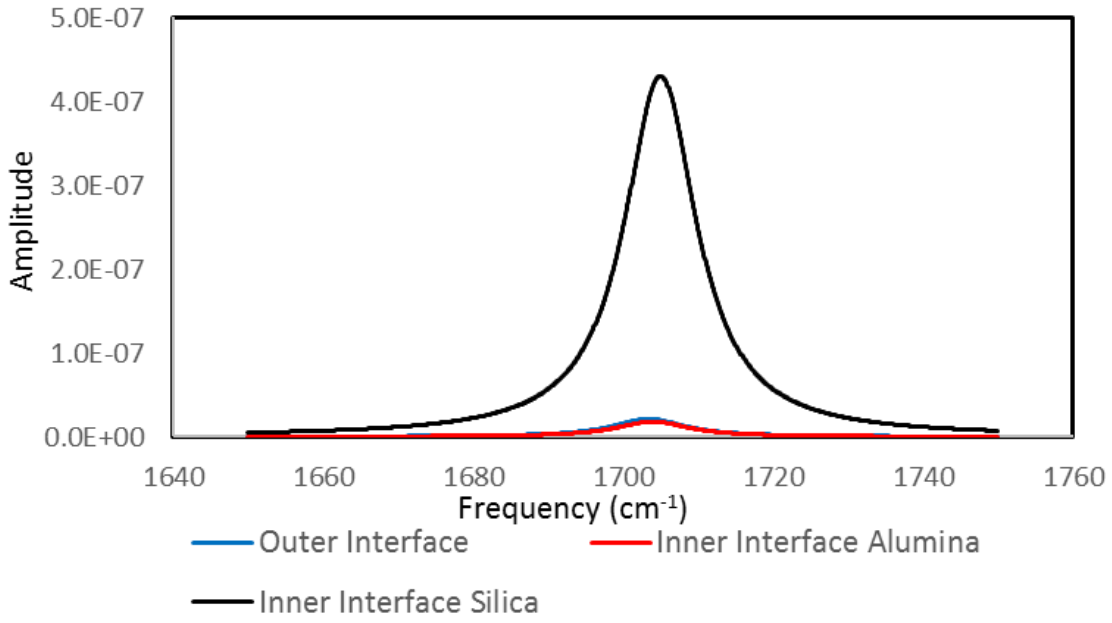

Figure 6.3: Absolute value of the resonant component of symmetric imide stretch for PTCDI on Al_2O_3 and SiO_2 in SSP configuration. Left panel has both outer and inner interface contributions, right panel has just the inner contributions for clarity.

Figure 6.3 shows the absolute values of the various symmetric resonant components with the SSP polarization combination. Note that the outer component and inner component on Al_2O_3 have similar amplitudes of 8.54×10^{-4} and 7.85×10^{-4}, respectively. The inner contribution for SiO_2 is much larger than either of these at 3.84×10^{-3}. The buried symmetric stretch for PPP on Al_2O_3 is orders of magnitude smaller at 1.40×10^{-9} compared to the SiO_2 data at 2.207×10^{-4}. The different amplitudes at the two different buried interfaces with different polarization combinations shows that the molecules are arranged differently at the Al_2O_3 interface than at the SiO_2 interface. It is generally understood that relative differences in SSP amplitudes can tell relatively how

a molecule how a dipole is sitting on a surface: the larger the SSP signal the more perpendicular or 'upright' the dipole is to the surface. In the case of PTCDI, this corresponds to a molecule standing up relatively end-on at the dielectric interface. The data here indicate that PTCDI sits on the surface more upright on SiO_2 than it does on Al_2O_3. This is significant and π-π overlap is important in how well the material behaves as a semiconductor; a more reclined position inhibits π-π stacking. Given that both the SSP and PPP data give much smaller intensities on Al_2O_3 than they do on SiO_2, it is also likely that the PTCDI is in general more disordered on Al_2O_3 than on SiO_2. Furthermore, comparing this material on the two different dielectrics by AFM shows that at the outer interface, they look largely the same, corroborating the claim that molecules at the buried interface arrange themselves differently for different dielectric environments.

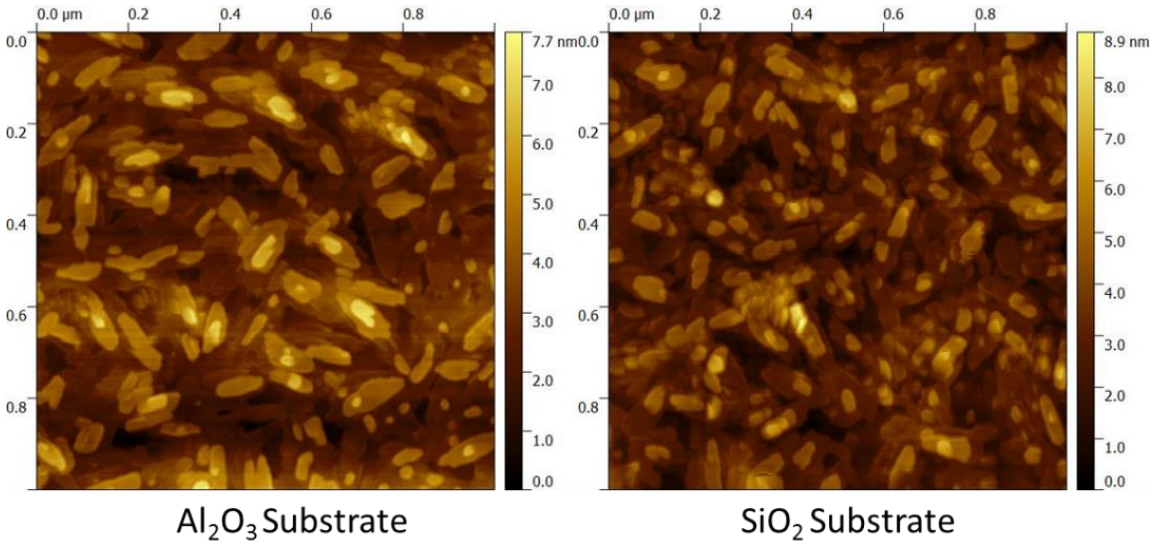

Figure 6.4: AFM of 20 nm of PTCDI on Al_2O_3 and SiO_2. Notice that while the grains are slightly smaller on the SiO_2 substrate, the topography is very similar.

None of the SPS data were able to be fit since many of the spectra had very low signal to noise (some gave nearly zero signal). This makes analysis difficult. Previous work done by O'Brien and coworkers showed that there were points in thickness of dielectric and PTCDI that the intensity of the SFG will go to zero by thin film interference effects. We are near these points for PTCDI on SiO_2, and could be in a similar place for Al_2O_3.[65]

6.4 Conclusions

It appears that the chemical environment felt by PTCDI is similar for both SiO_2 and Al_2O_3 given that the frequency of the buried modes stay the same. However, it is evident that the different dielectric surfaces affect interfacial order and orientation. As previously mentioned Veres and Coworkers postulated that a decrease in charge mobility for a given semiconductor on higher k dielectrics was due to a disordering effect from the higher polarity of the surface. Given the significantly decreased signal of the buried VSFG resonances this appears to indeed be the case. Furthermore, VSFG also showed that while there is more disorder it is also likely that PTCDI sits on the dielectric more reclined, leading to a decrease in charge mobility because of a lack of π-π stacking. This leads to the conclusion that while higher k dielectrics are useful in creating devices that are more efficient, due to decreased threshold voltage, surface treatment with SAMs are necessary to maintain adequate charge mobilities.

Furthermore, the thin film interference model predicts that varying the dielectric affects the observed VSFG spectra as much as the thickness of the material.[65] Given the great precision one can deposit dielectrics via ALD and other deposition methods, it is possible to use this methodology to find dielectric thicknesses that offer enormous

enhancement of the signal. This might be useful as there is growing evidence for phase changes of the buried interface as the thin film is grown thicker.[161]

It is also interesting that there was no non-resonant enhancement from the Al_2O_3 dielectric. It is possible that much larger thicknesses are necessary in order for this to become a more important part of the signal. Non-resonant backgrounds have been looked at as another way of determining VSFG phase information.[162-163] It is possible that when thin film interference effects are present, such as in these experiments and other involving multiple interfaces, the effects of non-resonant enhancement may be small in comparison to thin film interference effects.

Bibliography

1. Horowitz, G., Charge Transport in Oligomers. In *Organic Field-Effect Transistors*, Bao, Z.; Locklin, J., Eds. CRC Press: Boca Raton, FL, 2007; p 27.
2. Coropceanu, V.; Cornil, J.; da Silva, D. A.; Olivier, Y.; Silbey, R.; Bredas, J. L., Charge transport in organic semiconductors. *Chem. Rev.* **2007,** *107* (4), 926-952.
3. Bredas, J. L.; Calbert, J. P.; da Silva, D. A.; Cornil, J., Organic semiconductors: A theoretical characterization of the basic parameters governing charge transport. *Proc. Natl. Acad. Sci. U.S.A.* **2002,** *99* (9), 5804-5809.
4. Bredas, J. L.; Beljonne, D.; Coropceanu, V.; Cornil, J., Charge-transfer and energy-transfer processes in pi-conjugated oligomers and polymers: A molecular picture. *Chem. Rev.* **2004,** *104* (11), 4971-5003.
5. Lemaur, V.; Da Silva Filho, D. A.; Coropceanu, V.; Lehmann, M.; Geerts, Y.; Piris, J.; Debije, M. G.; Van de Craats, A. M.; Senthilkumar, K.; Siebbeles, L. D. A.; Warman, J. M.; Bredas, J. L.; Cornil, J., Charge transport properties in discotic liquid crystals: A quantum-chemical insight into structure-property relationships. *J. Am. Chem. Soc.* **2004,** *126* (10), 3271-3279.
6. Kwon, O.; Coropceanu, V.; Gruhn, N. E.; Durivage, J. C.; Laquindanum, J. G.; Katz, H. E.; Cornil, J.; Bredas, J. L., Characterization of the molecular parameters determining charge transport in anthradithiophene. *J. Chem. Phys.* **2004,** *120* (17), 8186-8194.
7. Horowitz, G., Organic field-effect transistors. *Adv. Mater.* **1998,** *10* (5), 365-377.
8. Silbey, R.; Munn, R. W., General-Theory of Electronic Transport in Molecular-Crystals .1. Local Linear Electron-Phonon Coupling. *J. Chem. Phys.* **1980,** *72* (4), 2763-2773.
9. Kenkre, V. M.; Andersen, J. D.; Dunlap, D. H.; Duke, C. B., Unified Theory of the Mobilities of Photoinjected Electrons in Napthalene. *Phys. Rev. Lett.* **1989,** *62* (10), 1165-1168.
10. Giuggioli, L.; Andersen, J. D.; Kenkre, V. M., Mobility theory of intermediate-bandwidth carriers in organic crystals: Scattering by acoustic and optical phonons. *Physical Review B* **2003,** *67* (4), 10.
11. Marcus, R. A., Electron-Transfer Reactions in Chemistry - Theory and Experiment. *Rev. Mod. Phys.* **1993,** *65* (3), 599-610.
12. Bassler, H., Charge-Transport in Random Organic Photoconductors. *Adv. Mater.* **1993,** *5* (9), 662-665.
13. Fishchuk, II; Arkhipov, V. I.; Kadashchuk, A.; Heremans, P.; Bassler, H., Analytic model of hopping mobility at large charge carrier concentrations in disordered organic semiconductors: Polarons versus bare charge carriers. *Physical Review B* **2007,** *76* (4), 12.
14. Arkhipov, V. I.; Heremans, P.; Emelianova, E. V.; Adriaenssens, G. J.; Bassler, H., Weak-field carrier hopping in disordered organic semiconductors: the effects of deep traps and partly filled density-of-states distribution. *Journal of Physics-Condensed Matter* **2002,** *14* (42), 9899-9911.
15. Mallik, A. B.; Locklin, J.; Mannsfeld, S. C. B.; Reese, C.; Roberts, M. E.; Senatore, M. L.; Zi, H.; Bao, Z., Design, Synthesis, and Transistor Perfomance of Organic Semiconductors. In *Organic Field-Effect Transistors*, Bao, Z.; Locklin, J., Eds. CRC Press: Boca Raton, FL, 2007; p 159.
16. de Boer, R. W. I.; Klapwijk, T. M.; Morpurgo, A. F., Field-effect transistors on tetracene single crystals. *Appl. Phys. Lett.* **2003,** *83* (21), 4345-4347.
17. Butko, V. Y.; Chi, X.; Lang, D. V.; Ramirez, A. P., Field-effect transistor on pentacene single crystal. *Appl. Phys. Lett.* **2003,** *83* (23), 4773-4775.

18. Hasegawa, T.; Takeya, J., Organic field-effect transistors using single crystals. *Science and Technology of Advanced Materials* **2009,** *10* (2), 16.
19. Griffith, O. L.; Anthony, J. E.; Jones, A. G.; Shu, Y.; Lichtenberger, D. L., Substituent Effects on the Electronic Characteristics of Pentacene Derivatives for Organic Electronic Devices: Dioxolane-Substituted Pentacene Derivatives with Triisopropylsilylethynyl Functional Groups. *J. Am. Chem. Soc.* **2012,** *134* (34), 14185-14194.
20. Anthony, J. E.; Brooks, J. S.; Eaton, D. L.; Parkin, S. R., Functionalized pentacene: Improved electronic properties from control of solid-state order. *J. Am. Chem. Soc.* **2001,** *123* (38), 9482-9483.
21. Brooks, J. S.; Eaton, D. L.; Anthony, J. E.; Parkin, S. R.; Brill, J. W.; Sushko, Y., Electronic and optical properties of functionalized pentacene compounds in the solid state. *Current Applied Physics* **2001,** *1* (4-5), 301-306.
22. Anthony, J. E.; Purushothaman, B., Crystal design for organic semicondutors: The effects of substitution on crystal packing. In *Organic Field-Effect Transistors Vi*, Bao, Z.; Gundlach, D. J., Eds. Spie-Int Soc Optical Engineering: Bellingham, 2007; Vol. 6658.
23. Wolak, M. A.; Delcamp, J.; Landis, C. A.; Lane, P. A.; Anthony, J.; Kafafi, Z., High-performance organic light-emitting diodes based on dioxolane-substituted pentacene derivatives. *Adv. Funct. Mater.* **2006,** *16* (15), 1943-1949.
24. Lim, Y. F.; Shu, Y.; Parkin, S. R.; Anthony, J. E.; Malliaras, G. G., Soluble n-type pentacene derivatives as novel acceptors for organic solar cells. *J. Mater. Chem.* **2009,** *19* (19), 3049-3056.
25. Yassar, A.; Demanze, F.; Jaafari, A.; El Idrissi, M.; Coupry, C., Cyano-substituted oligothiophenes: A new approach to n-type organic semiconductors. *Adv. Funct. Mater.* **2002,** *12* (10), 699-708.
26. Facchetti, A.; Deng, Y.; Wang, A. C.; Koide, Y.; Sirringhaus, H.; Marks, T. J.; Friend, R. H., Tuning the semiconducting properties of sexithiophene by alpha,omega-substitution - alpha,omega-diperfluorohexylsexithiophene: The first n-type sexithiophene for thin-film transistors. *Angewandte Chemie-International Edition* **2000,** *39* (24), 4547-+.
27. Facchetti, A.; Mushrush, M.; Katz, H. E.; Marks, T. J., n-type building blocks for organic electronics: A homologous family of fluorocarbon-substituted thiophene oligomers with high carrier mobility. *Adv. Mater.* **2003,** *15* (1), 33-+.
28. Facchetti, A.; Yoon, M. H.; Stern, C. L.; Hutchison, G. R.; Ratner, M. A.; Marks, T. J., Building blocks for N-type molecular and polymeric electronics. Perfluoroalkyl- versus alkyl-functionalized ligothiophenes (nTs; n=2-6). Systematic synthesis, spectroscopy, electrochemistry, and solid-state organization. *J. Am. Chem. Soc.* **2004,** *126* (41), 13480-13501.
29. Jones, B. A.; Facchetti, A.; Wasielewski, M. R.; Marks, T. J., Tuning orbital energetics in arylene diimide semiconductors. Materials design for ambient stability of n-type charge transport. *J. Am. Chem. Soc.* **2007,** *129* (49), 15259-15278.
30. Katz, H. E.; Lovinger, A. J.; Johnson, J.; Kloc, C.; Siegrist, T.; Li, W.; Lin, Y. Y.; Dodabalapur, A., A soluble and air-stable organic semiconductor with high electron mobility. *Nature* **2000,** *404* (6777), 478-481.
31. Usta, H.; Risko, C.; Wang, Z. M.; Huang, H.; Deliomeroglu, M. K.; Zhukhovitskiy, A.; Facchetti, A.; Marks, T. J., Design, Synthesis, and Characterization of Ladder-Type Molecules and Polymers. Air-Stable, Solution-Processable n-Channel and Ambipolar Semiconductors for Thin-Film Transistors via Experiment and Theory. *J. Am. Chem. Soc.* **2009,** *131* (15), 5586-5608.
32. Jones, B. A.; Ahrens, M. J.; Yoon, M. H.; Facchetti, A.; Marks, T. J.; Wasielewski, M. R., High-mobility air-stable n-type semiconductors with processing versatility: Dicyanoperylene-3,4 : 9,10-bis(dicarboximides). *Angewandte Chemie-International Edition* **2004,** *43* (46), 6363-6366.

33. Gao, X. K.; Di, C. A.; Hu, Y. B.; Yang, X. D.; Fan, H. Y.; Zhang, F.; Liu, Y. Q.; Li, H. X.; Zhu, D. B., Core-Expanded Naphthalene Diimides Fused with 2-(1,3-Dithiol-2-Ylidene)Malonitrile Groups for High-Performance, Ambient-Stable, Solution-Processed n-Channel Organic Thin Film Transistors. *J. Am. Chem. Soc.* **2010,** *132* (11), 3697-+.
34. Yamane, K.; Yanagi, H.; Hotta, S., Ambipolar field effect transistors with heterojunction of organic semiconductors. *Thin Solid Films* **2008,** *516* (10), 3157-3161.
35. He, Y. J.; Li, Y. F., Fullerene derivative acceptors for high performance polymer solar cells. *PCCP* **2011,** *13* (6), 1970-1983.
36. Dennler, G.; Scharber, M. C.; Brabec, C. J., Polymer-Fullerene Bulk-Heterojunction Solar Cells. *Adv. Mater.* **2009,** *21* (13), 1323-1338.
37. Katz, H. E.; Johnson, J.; Lovinger, A. J.; Li, W. J., Naphthalenetetracarboxylic diimide-based n-channel transistor semiconductors: Structural variation and thiol-enhanced gold contacts. *J. Am. Chem. Soc.* **2000,** *122* (32), 7787-7792.
38. Malenfant, P. R. L.; Dimitrakopoulos, C. D.; Gelorme, J. D.; Kosbar, L. L.; Graham, T. O.; Curioni, A.; Andreoni, W., N-type organic thin-film transistor with high field-effect mobility based on a N,N-'-dialkyl-3,4,9,10-perylene tetracarboxylic diimide derivative. *Appl. Phys. Lett.* **2002,** *80* (14), 2517-2519.
39. Briseno, A. L.; Mannsfeld, S. C. B.; Reese, C.; Hancock, J. M.; Xiong, Y.; Jenekhe, S. A.; Bao, Z.; Xia, Y. N., Perylenediimide nanowires and their use in fabricating field-effect transistors and complementary inverters. *Nano Lett.* **2007,** *7* (9), 2847-2853.
40. Wang, G. M.; Swensen, J.; Moses, D.; Heeger, A. J., Increased mobility from regioregular poly(3-hexylthiophene) field-effect transistors. *J. Appl. Phys.* **2003,** *93* (10), 6137-6141.
41. Sirringhaus, H.; Brown, P. J.; Friend, R. H.; Nielsen, M. M.; Bechgaard, K.; Langeveld-Voss, B. M. W.; Spiering, A. J. H.; Janssen, R. A. J.; Meijer, E. W.; Herwig, P.; de Leeuw, D. M., Two-dimensional charge transport in self-organized, high-mobility conjugated polymers. *Nature* **1999,** *401* (6754), 685-688.
42. Sirringhaus, H.; Tessler, N.; Friend, R. H., Integrated optoelectronic devices based on conjugated polymers. *Science* **1998,** *280* (5370), 1741-1744.
43. Panzer, M. J.; Frisbie, C. D., Contact Effects in Organic Field-Effect Transistors. In *Organic Field-Effect Transistors*, Bao, Z.; Locklin, J., Eds. CRC Press: Boca Raton, FL, 2007; p 139.
44. Knipp, D.; Street, R. A.; Volkel, A.; Ho, J., Pentacene thin film transistors on inorganic dielectrics: Morphology, structural properties, and electronic transport. *J. Appl. Phys.* **2003,** *93* (1), 347-355.
45. Fleischli, F. D.; Suárez, S. p.; Schaer, M.; Zuppiroli, L., Organic Thin-Film Transistors: The Passivation of the Dielectric-Pentacene Interface by Dipolar Self-Assembled Monolayers. *Langmuir* **2010,** *26* (18), 15044-15049.
46. Verlaak, S.; Arkhipov, V.; Heremans, P., Modeling of transport in polycrystalline organic semiconductor films. *Appl. Phys. Lett.* **2003,** *82* (5), 745-747.
47. Steudel, S.; De Vusser, S.; De Jonge, S.; Janssen, D.; Verlaak, S.; Genoe, J.; Heremans, P., Influence of the dielectric roughness on the performance of pentacene transistors. *Appl. Phys. Lett.* **2004,** *85* (19), 4400-4402.
48. Salleo, A.; Chabinyc, M. L.; Yang, M. S.; Street, R. A., Polymer thin-film transistors with chemically modified dielectric interfaces. *Appl. Phys. Lett.* **2002,** *81* (23), 4383-4385.
49. Kelley, T. W.; Boardman, L. D.; Dunbar, T. D.; Muyres, D. V.; Pellerite, M. J.; Smith, T. Y. P., High-performance OTFTs using surface-modified alumina dielectrics. *J. Phys. Chem. B* **2003,** *107* (24), 5877-5881.
50. Salinas, M.; Jaeger, C. M.; Amin, A. Y.; Dral, P. O.; Meyer-Friedrichsen, T.; Hirsch, A.; Clark, T.; Halik, M., The Relationship between Threshold Voltage and Dipolar Character of Self-

Assembled Monolayers in Organic Thin-Film Transistors. *J. Am. Chem. Soc.* **2012,** *134* (30), 12648-12652.
51. Jung, Y.; Kline, R. J.; Fischer, D. A.; Lin, E. K.; Heeney, M.; McCulloch, I.; DeLongchamp, D. M., The effect of interfacial roughness on the thin film morphology and charge transport of high-performance polythiophenes. *Adv. Funct. Mater.* **2008,** *18* (5), 742-750.
52. Puntambekar, K.; Dong, J. P.; Haugstad, G.; Frisbie, C. D., Structural and electrostatic complexity at a pentacene/insulator interface. *Adv. Funct. Mater.* **2006,** *16* (7), 879-884.
53. Kehrer, L. A.; Feldmeier, E. J.; Siol, C.; Walker, D.; Melzer, C.; von Seggern, H., A new method to invert top-gate organic field-effect transistors for Kelvin probe investigations. *Applied Physics a-Materials Science & Processing* **2013,** *112* (2), 431-436.
54. Muller, K.; Goryachko, A.; Burkov, Y.; Schwiertz, C.; Ratzke, M.; Koble, J.; Reif, J.; Schmeisser, D., Scanning Kelvin probe and photoemission electron microscopy of organic source-drain structures. *Synth. Met.* **2004,** *146* (3), 377-382.
55. Afsharimani, N.; Nysten, B., Scanning probe microscopy study of electronic properties in alkyl-substituted oligothiophene-based field-effect transitors. *Vacuum* **2013,** *90*, 17-24.
56. Nahid, M. M.; Gann, E.; Thomsen, L.; McNeill, C. R., NEXAFS spectroscopy of conjugated polymers. *Eur. Polym. J.* **2016,** *81*, 532-554.
57. Double, K. L.; Zecca, L.; Costi, P.; Mauer, M.; Griesinger, C.; Ito, S.; Ben-Shachar, D.; Bringmann, G.; Fariello, R. G.; Riederer, P.; Gerlach, M., Structural characteristics of human substantia nigra neuromelanin and synthetic dopamine melanins. *J. Neurochem.* **2000,** *75* (6), 2583-2589.
58. O'Brien, D. B.; Anglin, T. C.; Massari, A. M., Surface Chemistry and Annealing-Driven Interfacial Changes in Organic Semiconducting Thin Films on Silica Surfaces. *Langmuir* **2011,** *27* (22), 13940-13949.
59. Anglin, T. C.; Lane, A. P.; Massari, A. M., Real-time structural evolution at the interface of an organic transistor during thermal annealing. *Journal of Materials Chemistry C* **2014,** *2* (17), 3390-3400.
60. Anglin, T. C.; Sohrabpour, Z.; Massari, A. M., Nonlinear Spectroscopic Markers of Structural Change during Charge Accumulation in Organic Field-Effect Transistors. *Journal of Physical Chemistry C* **2011,** *115* (41), 20258-20266.
61. Anglin, T. C.; O'Brien, D. B.; Massari, A. M., Monitoring the Charge Accumulation Process in Polymeric Field-Effect Transistors via in Situ Sum Frequency Generation. *J. Phys. Chem. C* **2010,** *114* (41), 17629-17637.
62. Anglin, T. C.; O'Brien, D. B.; Massari, A. M., In-situ vibrational sum-frequency spectroscopy of the conduction channel in polymer field-effect transistors. *Abstr Pap Am Chem S* **2010,** *239*.
63. Anglin, T. C.; Speros, J. C.; Massari, A. M., VSFG determination of the interfacial orientation of poly(3-hexylthiophene) on modified oFET dielectrics and correlation to device electrical performance. *Abstr Pap Am Chem S* **2011,** *242*.
64. Anglin, T. C.; Speros, J. C.; Massari, A. M., Interfacial Ring Orientation in Polythiophene Field-Effect Transistors on Functionalized Dielectrics. *Journal of Physical Chemistry C* **2011,** *115* (32), 16027-16036.
65. O'Brien, D. B.; Massari, A. M., Experimental evidence for an optical interference model for vibrational sum frequency generation on multilayer organic thin film systems. I. Electric dipole approximation. *J. Chem. Phys.* **2015,** *142* (2).
66. O'Brien, D. B.; Massari, A. M., Experimental evidence for an optical interference model for vibrational sum frequency generation on multilayer organic thin film systems. II. Consideration for higher order terms. *J. Chem. Phys.* **2015,** *142* (2).

67. Ye, H.; Huang, J.; Park, J. R.; Katz, H. E.; Gracias, D. H., Correlations between SFG spectra and electrical properties of organic field effect transistors. *Journal of Physical Chemistry C* **2007,** *111* (35), 13250-13255.
68. Ye, H. K.; Abu-Akeel, A.; Huang, J.; Katz, H. E.; Gracias, D. H., Probing organic field effect transistors in situ during operation using SFG. *J. Am. Chem. Soc.* **2006,** *128* (20), 6528-6529.
69. Walter, S. R.; Youn, J.; Emery, J. D.; Kewalramani, S.; Hennek, J. W.; Bedzyk, M. J.; Facchetti, A.; Marks, T. J.; Geiger, F. M., In-Situ Probe of Gate Dielectric-Semiconductor Interfacial Order in Organic Transistors: Origin and Control of Large Performance Sensitivities. *J. Am. Chem. Soc.* **2012,** *134* (28), 11726-11733.
70. Lambert, A. G.; Davies, P. B.; Neivandt, D. J., Implementing the theory of sum frequency generation vibrational spectroscopy: A tutorial review. *Appl. Spectrosc. Rev.* **2005,** *40* (2), 103-145.
71. Shen, Y. R., *The Principles of Nonlinear Optics*. John Wiley and Sons, Inc.: 1984.
72. Moad, A. J.; Simpson, G. J., A unified treatment of selection rules and symmetry relations for sum-frequency and second harmonic spectroscopies. *J. Phys. Chem. B* **2004,** *108* (11), 3548-3562.
73. Wang, H. F.; Gan, W.; Lu, R.; Rao, Y.; Wu, B. H., Quantitative spectral and orientational analysis in surface sum frequency generation vibrational spectroscopy (SFG-VS). *Int. Rev. Phys. Chem.* **2005,** *24* (2), 191-256.
74. O'Brien, D. B. Solving the two-interface problem in vibrational sum frequency generation spectroscopy applied to multilayer thin film systems. University of Minnesota - Twin Cities, Minneapolis, 2014.
75. O'Brien, D. B.; Massari, A. M., Modeling multilayer thin film interference effects in interface-specific coherent nonlinear optical spectroscopies. *Journal of the Optical Society of America B-Optical Physics* **2013,** *30* (6), 1503-1512.
76. O'Brien, D. B.; Massari, A. M., Simulated vibrational sum frequency generation from a multilayer thin film system with two active interfaces. *J. Chem. Phys.* **2013,** *138* (15).
77. Cosandey, F.; Madey, T. E., Growth, morphology, interfacial effects and catalytic properties of Au on TiO2. *Surf. Rev. Lett.* **2001,** *8* (1-2), 73-93.
78. Hansen, P. L.; Wagner, J. B.; Helveg, S.; Rostrup-Nielsen, J. R.; Clausen, B. S.; Topsoe, H., Atom-resolved imaging of dynamic shape changes in supported copper nanocrystals. *Science* **2002,** *295* (5562), 2053-2055.
79. Kim, M. S.; Rodriguez, N. M.; Baker, R. T. K., The Role of Interfacial Phenomena in the Structure of Carbon Deposits. *J. Catal.* **1992,** *134* (1), 253-268.
80. Maldonado, S.; Morin, S.; Stevenson, K. J., Structure, composition, and chemical reactivity of carbon nanotubes by selective nitrogen doping. *Carbon* **2006,** *44* (8), 1429-1437.
81. Gong, J. R.; Wan, L. J.; Lei, S. B.; Bai, C. L.; Zhang, X. H.; Lee, S. T., Direct evidence of molecular aggregation and degradation mechanism of organic light-emitting diodes under joule heating: an STM and photoluminescence study. *J. Phys. Chem. B* **2005,** *109* (5), 1675-1682.
82. Griffith, M. J.; Sunahara, K.; Wagner, P.; Wagner, K.; Wallace, G. G.; Officer, D. L.; Furube, A.; Katoh, R.; Mori, S.; Mozer, A. J., Porphyrins for dye-sensitised solar cells: new insights into efficiency-determining electron transfer steps. *Chem. Commun.* **2012,** *48* (35), 4145-4162.
83. Moser, J.; Punchihewa, S.; Infelta, P. P.; Gratzel, M., Surface Complexation of Colloidal Semiconductors Strongly Enhances Interfacial Electron-Transfer Rates. *Langmuir* **1991,** *7* (12), 3012-3018.
84. Cornil, J.; Beljonne, D.; Calbert, J. P.; Bredas, J. L., Interchain interactions in organic pi-conjugated materials: Impact on electronic structure, optical response, and charge transport. *Adv. Mater.* **2001,** *13* (14), 1053-1067.

85. Nguyen, C. N.; Stratt, R. M., Preferential solvation dynamics in liquids: How geodesic pathways through the potential energy landscape reveal mechanistic details about solute relaxation in liquids. *J. Chem. Phys.* **2010,** *133* (12), 124503.
86. Stratt, R. M.; Maroncelli, M., Nonreactive dynamics in solution: The emerging molecular view of solvation dynamics and vibrational relaxation. *J. Phys. Chem.* **1996,** *100* (31), 12981-12996.
87. Jones, B. H.; Huber, C. J.; Spector, I. C.; Tabet, A. M.; Butler, R. L.; Hang, Y.; Massari, A. M., Correlating solvent dynamics and chemical reaction rates using binary solvent mixtures and two-dimensional infrared spectroscopy. *J. Chem. Phys.* **2015,** *142* (21), 212441.
88. Gopalakrishnan, S.; Liu, D. F.; Allen, H. C.; Kuo, M.; Shultz, M. J., Vibrational spectroscopic studies of aqueous interfaces: Salts, acids, bases, and nanodrops. *Chem. Rev.* **2006,** *106* (4), 1155-1175.
89. Nihonyanagi, S.; Ishiyama, T.; Lee, T.; Yamaguchi, S.; Bonn, M.; Morita, A.; Tahara, T., Unified Molecular View of the Air/Water Interface Based on Experimental and Theoretical chi((2)) Spectra of an Isotopically Diluted Water Surface. *J. Am. Chem. Soc.* **2011,** *133* (42), 16875-16880.
90. Nihonyanagi, S.; Yamaguchi, S.; Tahara, T., Direct evidence for orientational flip-flop of water molecules at charged interfaces: A heterodyne-detected vibrational sum frequency generation study. *J. Chem. Phys.* **2009,** *130* (20), 204704.
91. Richmond, G. L., Molecular bonding and interactions at aqueous surfaces as probed by vibrational sum frequency spectroscopy. *Chem. Rev.* **2002,** *102* (8), 2693-2724.
92. Stiopkin, I. V.; Weeraman, C.; Pieniazek, P. A.; Shalhout, F. Y.; Skinner, J. L.; Benderskii, A. V., Hydrogen bonding at the water surface revealed by isotopic dilution spectroscopy. *Nature* **2011,** *474* (7350), 192-195.
93. Lu, R.; Gan, W.; Wu, B. H.; Zhang, Z.; Guo, Y.; Wang, H. F., C-H stretching vibrations of methyl, methylene and methine groups at the vapor/alcohol (n=1-8) interfaces. *J. Phys. Chem. B* **2005,** *109* (29), 14118-14129.
94. Aliaga, C.; Santos, C. S.; Baldelli, S., Surface chemistry of room-temperature ionic liquids. *PCCP* **2007,** *9* (28), 3683-3700.
95. Bain, C. D., Sum-Frequency Vibrational Spectroscopy of the Solid-Liquid Interface. *Journal of the Chemical Society-Faraday Transactions* **1995,** *91* (9), 1281-1296.
96. Brindza, M. R.; Walker, R. A., Differentiating Solvation Mechanisms at Polar Solid/Liquid Interfaces. *J. Am. Chem. Soc.* **2009,** *131* (17), 6207-6214.
97. Jena, K. C.; Hore, D. K., Variation of Ionic Strength Reveals the Interfacial Water Structure at a Charged Mineral Surface. *Journal of Physical Chemistry C* **2009,** *113* (34), 15364-15372.
98. Kim, J.; Kim, G.; Cremer, P. S., Investigations of water structure at the solid/liquid interface in the presence of supported lipid bilayers by vibrational sum frequency spectroscopy. *Langmuir* **2001,** *17* (23), 7255-7260.
99. Lu, G. Q.; Lagutchev, A.; Dlott, D. D.; Wieckowski, A., Quantitative vibrational sum-frequency generation spectroscopy of thin layer electrochemistry: CO on a Pt electrode. *Surf. Sci.* **2005,** *585* (1-2), 3-16.
100. Roke, S.; Kleyn, A. W.; Bonn, M., Femtosecond sum frequency generation at the metal-liquid interface. *Surf. Sci.* **2005,** *593* (1-3), 79-88.
101. Baldelli, S., Surface structure at the ionic liquid-electrified metal interface. *Acc. Chem. Res.* **2008,** *41* (3), 421-431.

102. Bonn, M.; Bakker, H. J.; Ghosh, A.; Yamamoto, S.; Sovago, M.; Campen, R. K., Structural Inhomogeneity of Interfacial Water at Lipid Monolayers Revealed by Surface-Specific Vibrational Pump-Probe Spectroscopy. *J. Am. Chem. Soc.* **2010,** *132* (42), 14971-14978.
103. Fu, L.; Ma, G.; Yan, E. C. Y., In Situ Misfolding of Human Islet Amyloid Polypeptide at Interfaces Probed by Vibrational Sum Frequency Generation. *J. Am. Chem. Soc.* **2010,** *132* (15), 5405-5412.
104. Liu, J.; Conboy, J. C., Phase transition of a single lipid bilayer measured by sum-frequency vibrational spectroscopy. *J. Am. Chem. Soc.* **2004,** *126* (29), 8894-8895.
105. Haupert, L. M.; Simpson, G. J., Chirality in Nonlinear Optics. *Annu. Rev. Phys. Chem.* **2009,** *60*, 345-365.
106. Jubb, A. M.; Hua, W.; Allen, H. C., Environmental Chemistry at Vapor/Water Interfaces: Insights from Vibrational Sum Frequency Generation Spectroscopy. *Annu. Rev. Phys. Chem.* **2012,** *63*, 107-130.
107. Stokes, G. Y.; Buchbinder, A. M.; Gibbs-Davis, J. M.; Scheidt, K. A.; Geiger, F. M., Heterogeneous Ozone Oxidation Reactions of 1-Pentene, Cyclopentene, Cyclohexene, and a Menthenol Derivative Studied by Sum Frequency Generation. *J. Phys. Chem. A* **2008,** *112* (46), 11688-11698.
108. Zhang, C.; Jasensky, J.; Leng, C.; Del Grosso, C.; Smith, G. D.; Wilker, J. J.; Chen, Z., Sum frequency generation vibrational spectroscopic studies on buried heterogeneous biointerfaces. *Opt. Lett.* **2014,** *39* (9), 2715-2718.
109. Gautam, K. S.; Schwab, A. D.; Dhinojwala, A.; Zhang, D.; Dougal, S. M.; Yeganeh, M. S., Molecular structure of polystyrene at air/polymer and solid/polymer interfaces. *Phys. Rev. Lett.* **2000,** *85* (18), 3854-3857.
110. Li, G. F.; Dhinojwala, A.; Yeganeh, M. S., Interference Effect from Buried Interfaces Investigated by Angular-Dependent Infrared-Visible Sum Frequency Generation Technique. *Journal of Physical Chemistry C* **2011,** *115* (15), 7554-7561.
111. Harp, G. P.; Gautam, K. S.; Dhinojwala, A., Probing polymer/polymer interfaces. *J. Am. Chem. Soc.* **2002,** *124* (27), 7908-7909.
112. Li, G.; Dhinojwala, A.; Yeganeh, M. S., Interfacial Structure and Melting Temperature of Alcohol and Alkane Molecules in Contact with Polystyrene Films. *J. Phys. Chem. B* **2009,** *113* (9), 2739-2747.
113. Bao, Z. A.; Locklin, J., *Organic Field-Effect Transistors*. CRC Press: Boca Raton, 2007.
114. Chin, X. Y.; Yin, J.; Wang, Z.; Caironi, M.; Soci, C., Mapping polarons in polymer FETs by charge modulation microscopy in the mid-infrared. *Scientific Reports* **2014,** *4*.
115. Fraleoni-Morgera, A.; Tessarolo, M.; Perucchi, A.; Baldassarre, L.; Lupi, S.; Fraboni, B., Polarized Infrared Studies on Charge Transport in 4-Hydroxycyanobenzene Single Crystals. *Journal of Physical Chemistry C* **2012,** *116* (3), 2563-2569.
116. Kim, J.; Jung, S.; Choi, E. J.; Kim, K.; Lee, K.; Im, S., Infrared spectroscopy of the interface charge in a ZnO field-effect transistor. *Appl. Phys. Lett.* **2008,** *93* (24).
117. Kaake, L. G.; Zou, Y.; Panzer, M. J.; Frisbie, C. D.; Zhu, X., Vibrational spectroscopy reveals electrostatic and electrochemical doping in organic thin film transistors gated with a polymer electrolyte dielectric. *J. Am. Chem. Soc.* **2007,** *129* (25), 7824-7830.
118. Frisch, M. J.; Trucks, G. W.; Schlegel, H. B.; Scuseria, G. E.; Robb, M. A.; Cheeseman, J. R.; Scalmani, G.; Barone, V.; Mennucci, B.; Petersson, G. A.; Nakatsuji, H.; Caricato, M.; Li, X.; Hratchian, H. P.; Izmaylov, A. F.; Bloino, J.; Zheng, G.; Sonnenberg, J. L.; Hada, M.; Ehara, M.; Toyota, K.; Fukuda, R.; Hasegawa, J.; Ishida, M.; Nakajima, T.; Honda, Y.; Kitao, O.; Nakai, H.; Vreven, T.; Montgomery Jr., J. A.; Peralta, J. E.; Ogliaro, F.; Bearpark, M. J.; Heyd, J.; Brothers, E. N.; Kudin, K. N.; Staroverov, V. N.; Kobayashi, R.; Normand, J.; Raghavachari, K.; Rendell, A. P.;

Burant, J. C.; Iyengar, S. S.; Tomasi, J.; Cossi, M.; Rega, N.; Millam, N. J.; Klene, M.; Knox, J. E.; Cross, J. B.; Bakken, V.; Adamo, C.; Jaramillo, J.; Gomperts, R.; Stratmann, R. E.; Yazyev, O.; Austin, A. J.; Cammi, R.; Pomelli, C.; Ochterski, J. W.; Martin, R. L.; Morokuma, K.; Zakrzewski, V. G.; Voth, G. A.; Salvador, P.; Dannenberg, J. J.; Dapprich, S.; Daniels, A. D.; Farkas, Ö.; Foresman, J. B.; Ortiz, J. V.; Cioslowski, J.; Fox, D. J. *Gaussian 09 Revision D.01*, Gaussian, Inc.: Wallingford, CT, USA, 2009.

119. Hirshfeld, F. L., Bonded-Atom Fragments for Describing Molecular Charge-Densities. *Theor. Chim. Acta* **1977,** *44* (2), 129-138.

120. Marenich, A. V.; Jerome, S. V.; Cramer, C. J.; Truhlar, D. G., Charge Model 5: An Extension of Hirshfeld Population Analysis for the Accurate Description of Molecular Interactions in Gaseous and Condensed Phases. *Journal of Chemical Theory and Computation* **2012,** *8* (2), 527-541.

121. Ritchie, J. P., Electron-Density Distrobution Analysis for Nitromethane, Niromethide, and Nitramide. *J. Am. Chem. Soc.* **1985,** *107* (7), 1829-1837.

122. Ritchie, J. P.; Bachrach, S. M., Some Methods and Applications of Electron-Density Distribution Analysis. *J. Comput. Chem.* **1987,** *8* (4), 499-509.

123. Manaka, T.; Liu, F.; Weis, M.; Iwamoto, M., Mobility Measurement Based on Visualized Electric Field Migration in Organic Field-Effect Transistors. *Applied Physics Express* **2009,** *2* (6), 061501.

124. Manaka, T.; Liu, F.; Weis, M.; Iwamoto, M., Studying Transient Carrier Behaviors in Pentacene Field Effect Transistors Using Visualized Electric Field Migration. *Journal of Physical Chemistry C* **2009,** *113* (23), 10279-10284.

125. Ong, S. W.; Zhao, X. L.; Eisenthal, K. B., Polarization of Water-Molecules at a Charged Interface - 2nd Harmonic Studies of the Silica Water Interface. *Chem. Phys. Lett.* **1992,** *191* (3-4), 327-335.

126. Yamada, D.; Manaka, T.; Lim, E.; Tamura, R.; Weis, M.; Iwamoto, M., Injected carrier distribution in a pentacene field effect transistor probed using optical second harmonic generation. *J. Appl. Phys.* **2008,** *104* (7).

127. Rusanov, A. I., Surface thermodynamics revisited. *Surf. Sci. Rep.* **2005,** *58* (5-8), 111-239.

128. Slater, A. G.; Davies, E. S.; Argent, S. P.; Lewis, W.; Blake, A. J.; McMaster, J.; Champness, N. R., Bis-thioether-Substituted Perylene Diimides: Structural, Electrochemical, and Spectroelectrochemical Properties. *J. Org. Chem.* **2013,** *78* (7), 2853-2862.

129. Chis, V.; Mile, G.; Stiufiuc, R.; Leopold, N.; Oltean, M., Vibrational and electronic structure of PTCDI and melamine-PTCDI complexes. *J. Mol. Struct.* **2009,** *924-26*, 47-53.

130. Friedrich, M.; Gavrila, G.; Himcinschi, C.; Kampen, T. U.; Kobitski, A. Y.; Mendez, H.; Salvan, G.; Cerrillo, I.; Mendez, J.; Nicoara, N.; Baro, A. M.; Zahn, D. R. T., Optical properties and molecular orientation in organic thin films. *Journal of Physics-Condensed Matter* **2003,** *15* (38), S2699-S2718.

131. Andersson, M. P.; Uvdal, P., New scale factors for harmonic vibrational frequencies using the B3LYP density functional method with the triple-xi basis set 6-311+G(d,p). *J. Phys. Chem. A* **2005,** *109* (12), 2937-2941.

132. Nanova, D.; Beck, S.; Fuchs, A.; Glaser, T.; Lennartz, C.; Kowalsky, W.; Pucci, A.; Kroeger, M., Charge transfer in thin films of donor-acceptor complexes studied by infrared spectroscopy. *Org. Electron.* **2012,** *13* (7), 1237-1244.

133. Chesterfield, R. J.; McKeen, J. C.; Newman, C. R.; Ewbank, P. C.; da Silva, D. A.; Bredas, J. L.; Miller, L. L.; Mann, K. R.; Frisbie, C. D., Organic thin film transistors based on N-alkyl perylene diimides: Charge transport kinetics as a function of gate voltage and temperature. *J. Phys. Chem. B* **2004,** *108* (50), 19281-19292.

134. Krauss, T. N.; Barrena, E.; de Oteyza, D. G.; Zhang, X. N.; Major, J.; Dehm, V.; Wurthner, F.; Dosch, H., X-ray/Atomic Force Microscopy Study of the Temperature-Dependent Multilayer Structure of PTCDI-C-8 Films on SiO2. *Journal of Physical Chemistry C* **2009,** *113* (11), 4502-4506.
135. Dhar, P.; Khlyabich, P. P.; Burkhart, B.; Roberts, S. T.; Malyk, S.; Thompson, B. C.; Benderskii, A. V., Annealing-Induced Changes in the Molecular Orientation of Poly-3-hexylthiophene at Buried Interfaces. *Journal of Physical Chemistry C* **2013,** *117* (29), 15213-15220.
136. Simpson, G. J.; Rowlen, K. L., An SHG magic angle: Dependence of second harmonic generation orientation measurements on the width of the orientation distribution. *J. Am. Chem. Soc.* **1999,** *121* (11), 2635-2636.
137. Stiopkin, I. V.; Jayathilake, H. D.; Bordenyuk, A. N.; Benderskii, A. V., Heterodyne-detected vibrational sum frequency generation spectroscopy. *J. Am. Chem. Soc.* **2008,** *130* (7), 2271-2275.
138. Humbert, C.; Caudano, Y.; Dreesen, L.; Sartenaer, Y.; Mani, A. A.; Silien, C.; Lemaire, J. J.; Thiry, P. A.; Peremans, A., Self-assembled organic and fullerene monolayers characterisation by two-colour SFG spectroscopy: a pathway to meet doubly resonant SFG process. *Appl. Surf. Sci.* **2004,** *237* (1-4), 462-468.
139. Sohrabpour, Z.; Kearns, P. M.; Massari, A. M., Vibrational Sum Frequency Generation Spectroscopy of Fullerene at Dielectric Interfaces. *J. Phys. Chem. C* **2016,** *120* (3), 1666-1672.
140. Miranda, P. B.; Pflumio, V.; Saijo, H.; Shen, Y. R., Conformation of surfactant monolayers at solid/liquid interfaces. *Chem. Phys. Lett.* **1997,** *264* (3-4), 387-392.
141. Cimatu, K.; Baldelli, S., Sum frequency generation microscopy of microcontact-printed mixed self-assembled monolayers. *J. Phys. Chem. B* **2006,** *110* (4), 1807-1813.
142. Wei, Q. S.; Tajima, K.; Tong, Y. J.; Ye, S.; Hashimoto, K., Surface-Segregated Monolayers: A New Type of Ordered Monolayer for Surface Modification of Organic Semiconductors. *J. Am. Chem. Soc.* **2009,** *131* (48), 17597-17604.
143. Anglin, T. C.; Massari, A. M., Polarization-multiplexed vibrational sum frequency generation for comprehensive simultaneous characterization of interfaces. *Opt. Lett.* **2012,** *37* (10), 1754-1756.
144. Smits, M.; Sovago, M.; Wurpel, G. W. H.; Kim, D.; Muller, M.; Bonn, M., Polarization-resolved broad-bandwidth sum-frequency generation spectroscopy of monolayer relaxation. *Journal of Physical Chemistry C* **2007,** *111* (25), 8878-8883.
145. McDermott, M. L.; Petersen, P. B., Robust Self-Referencing Method for Chiral Sum Frequency Generation Spectroscopy. *J. Phys. Chem. B* **2015,** *119* (38), 12417-12423.
146. Martinez, O. E.; Gordon, J. P.; Fork, R. L., Negative Group-Velocity Dispersion Using Refraction. *J. Opt. Soc. Am. A* **1984,** *1* (10), 1003-1006.
147. Weiner, A. M., Ultrafast optical pulse shaping: A tutorial review. *Opt. Commun.* **2011,** *284* (15), 3669-3692.
148. Lagutchev, A.; Hambir, S. A.; Dlott, D. D., Nonresonant background suppression in broadband vibrational sum-frequency generation spectroscopy. *Journal of Physical Chemistry C* **2007,** *111* (37), 13645-13647.
149. Pernstich, K. P.; Haas, S.; Oberhoff, D.; Goldmann, C.; Gundlach, D. J.; Batlogg, B.; Rashid, A. N.; Schitter, G., Threshold voltage shift in organic field effect transistors by dipole monolayers on the gate insulator. *J. Appl. Phys.* **2004,** *96* (11), 6431-6438.
150. Chung, Y.; Verploegen, E.; Vailionis, A.; Sun, Y.; Nishi, Y.; Murmann, B.; Bao, Z., Controlling Electric Dipoles in Nanodielectrics and Its Applications for Enabling Air-Stable n-Channel Organic Transistors. *Nano Lett.* **2011,** *11* (3), 1161-1165.

151. Maliakal, A., Dielectric Materials: Selection and Design. In *Organic Field-Effect Transistors*, Bao, Z.; Locklin, J., Eds. CRC Press: Boca Raton, FL, 2007; p 229.
152. Na, H.; Shin, T. J.; Sim, K.; Chirawatkul, P.; Kim, S.; Heo, K. J.; Kim, S. J.; Pyo, S., Growth of n-type organic semiconductor for low-voltage transistors based on an ALD grown Al2O3 gate dielectric. *Synth. Met.* **2013,** *185*, 103-108.
153. Groner, M. D.; Elam, J. W.; Fabreguette, F. H.; George, S. M., Electrical characterization of thin Al2O3 films grown by atomic layer deposition on silicon and various metal substrates. *Thin Solid Films* **2002,** *413* (1-2), 186-197.
154. Groner, M. D.; Fabreguette, F. H.; Elam, J. W.; George, S. M., Low-temperature Al2O3 atomic layer deposition. *Chem. Mater.* **2004,** *16* (4), 639-645.
155. Fumagalli, L.; Natali, D.; Sampietro, M.; Peron, E.; Perissinotti, F.; Tallarida, G.; Ferrari, S., Al2O3 as gate dielectric for organic transistors: Charge transport phenomena in poly-(3-hexylthiophene) based devices. *Org. Electron.* **2008,** *9* (2), 198-208.
156. Veres, J.; Ogier, S. D.; Leeming, S. W.; Cupertino, D. C.; Khaffaf, S. M., Low-k insulators as the choice of dielectrics in organic field-effect transistors. *Adv. Funct. Mater.* **2003,** *13* (3), 199-204.
157. Dodge, M. J., Refractive Index. In *Handbook of Laser Science and Technology, Volume IV, Optical Materials: Part 2.*, CRC PRess: Boca Raton, 1986; p 30.
158. Malitson, I. H.; Dodge, M. J., Refractive Index and Birefringence of Synthetic Sapphire. *J. Opt. Soc. Am.* **1972,** *62*, 1405.
159. Kischkat, J.; Peters, S.; Gruska, B.; Semtsiv, M.; Chashnikova, M.; Klinkmuller, M.; Fedosenko, O.; Machulik, S.; Aleksandrova, A.; Monastyrskyi, G.; Flores, Y.; Masselink, W. T., Mid-infrared optical properties of thin films of aluminum oxide, titanium dioxide, silicon dioxide, aluminum nitride, and silicon nitride. *Appl. Opt.* **2012,** *51* (28), 6789-6798.
160. Kearns, P. M.; O'Brien, D. B.; Massari, A. M., Optical Interference Enhances Nonlinear Spectroscopic Sensitivity: When Light Gives You Lemons, Model Lemonade. *Journal of Physical Chemistry Letters* **2016,** *7* (1), 62-68.
161. Sandberg, H. G. O.; Frey, G. L.; Shkunov, M. N.; Sirringhaus, H.; Friend, R. H.; Nielsen, M. M.; Kumpf, C., Ultrathin regioregular poly(3-hexyl thiophene) field-effect transistors. *Langmuir* **2002,** *18* (26), 10176-10182.
162. Sovago, M.; Vartiainen, E.; Bonn, M., Determining Absolute Molecular Orientation at Interfaces: A Phase Retrieval Approach for Sum Frequency Generation Spectroscopy. *Journal of Physical Chemistry C* **2009,** *113* (15), 6100-6106.
163. Averett, S. C.; Calchera, A. R.; Patterson, J. E., Polarization and phase characteristics of nonresonant sum-frequency generation response from a silicon (111) surface. *Opt. Lett.* **2015,** *40* (21), 4879-4882.